SIAM J. APPL. MATH.
Vol. 0, No. 0, pp. 000–000


# PHASE-FIELD MODELS FOR BIOFILMS. I. THEORY AND 1-D SIMULATIONS*

TIANYU ZHANG†, N. G. COGAN†, AND QI WANG†

**Abstract.** We derive a set of phase field models for biofilms using the one-fluid two-component formulation in which the combination of extracellular polymeric substances (EPS, or polymer networks) and the bacteria is effectively modeled as one fluid component, while the collective ensemble of nutrient substrates and the solvent are modeled as the other. The biofilm is assumed to be an incompressible continuum, in which the ~~relative~~ motion of the polymer network and the solvent relative to the average velocity is accounted for by binary mixing kinetics. Various constitutive stress models are proposed for the effective polymer network component according to the property of the polymer network. Steady states are identified, their stability is analyzed (where two long wave growth modes are identified), and numerical solutions of different variations of the model in one space dimension are discussed and compared.

**Key words.** biofilms, Cahn–Hilliard equation, finite difference scheme, phase-field, polymer networks, steady states, stability

**AMS subject classifications.** AU TO PROVIDE

**DOI.** 10.1137/070691966

## 1. Introduction.

Biofilms are ubiquitous in natural and industrial settings. They exist on wet surfaces and consist of myriad microbes, their byproducts, and trapped particles. A biofilm community can be formed by a single bacterial species, but in nature biofilms almost always consist of rich mixtures of many species of bacteria, as well as fungi, algae, yeasts, protozoa, other microorganisms, debris, and corrosion products. Biofilms are held together primarily by polysaccharides and other long chain molecules, collectively termed "extracellular polymeric substances" or EPS. The bacteria cells produce the EPS and are held together by EPS strands, allowing them to develop complex, three-dimensional, resilient, attached communities [7, 9, 11, 12, 19, 20, 21, 26].

The Center for Disease Control and National Institutes of Health recently estimated that 65% to 85% of all chronic infections can be attributed to bacterial biofilms [10]. In human diseases, biofilm infections are some of the most difficult to treat. Even with rigorous antibiotic regimens, some biofilms, such as those within the thick airway mucus of cystic fibrosis (CF) patients, persist throughout the course of the disease process [17]. Bacterial biofilms can also be utilized in bioterrorism in which persistent "bioterrorist agent biofilms" formed by *Francisella tularensis* can grow on surfaces where environmental amoebas can phagocytose them, allowing for growth of fibrosis [17].

Biofilms cost the U.S. literally billions of dollars every year in energy losses, equipment damage, product contamination, and medical infections. Understanding the dynamics of the growth, transport, and destruction of biofilms is important for improving water treatment and medical treatment of diseases, protecting equipment

*Received by the editors May 15, 2007; accepted for publication (in revised form) April 15, 2008; published electronically DATE. This work supported by the Air Force Office of Scientific Research, Air Force Materials Command, USAF, under grant number F49550-05-1-0025 and the National Science Foundation through grants DMS-0605029, DMS-0626180 and DMS-0548511.
http://www.siam.org/journals/siap/x-x/69196.html
†Department of Mathematics, Florida State University, Tallahassee, FL 32306-4510 (zhang@math.fsu.edu, cogan@math.fsu.edu, wang@math.fsu.edu).

or devices from corrosion, and even preventing bioterrorism. The improved understanding of biofilms will have a significant impact on environmental sciences, medicine, civil engineering, naval sciences, military applications, and homeland security.

There have been increasing efforts to model biofilm structures and dynamics over the last two decades [27, 28, 29, 30], in which methods based on cellular automata, particle-based methods, continuum models, and multispecies modeling are attempted [1, 13, 22, 23, 32]. Recently Cogan and Keener developed a two-fluid model for biofilms, treating bacteria as a part of the polymer network [7]. The nutrient substrate is also treated passively as a part of the solvent. This work extended the polymeric mixture models of Tanaka [31] and Milner [25] and the work of Wolgemuth and et al. [33] for biological material mixtures. Similar multifluid modeling extension has also been done by Klapper and colleagues [1, 22].

We briefly recall the multifluid theory of Cogan and Keener for biofilms next. Let $\phi_n$ be the volume fraction of the polymer network, $\phi_s$ that of the solvent, $\mathbf{v}_n$ the velocity of the polymer network, $\mathbf{v}_s$ the velocity of the solvent, $c$ the concentration of the nutrient substrate, $p$ the pressure, and $\tau_n$ and $\tau_s$ the network and solvent stress tensor, respectively. In the Cogan–Keener model, the substrate is passively treated as a part of the solvent. This two-fluid model consists of the linear momentum balance equation for each fluid, where inertia for all species are ignored, and the transport equation for the nutrient concentration as well as the volume fraction of the polymer network [7].

The momentum balance equation for each species is respectively given by

$$\begin{aligned} \nabla\cdot(\phi_n\tau_n) - h_f\phi_n\phi_s(\mathbf{v}_n-\mathbf{v}_s) - \nabla\Psi - \phi_n\nabla p = 0,\\ \nabla\cdot(\phi_s\tau_s) - h_f\phi_n\phi_s(\mathbf{v}_n-\mathbf{v}_s) - \phi_s\nabla p = 0, \end{aligned} \tag{1.1}$$

where $h_f$ is the coefficient of friction and $\Psi$ is the osmotic pressure due to the existence of the polymer network; the transport equation of the polymer volume fraction and the conservation of the volume fraction for the solvent are given respectively by

$$\begin{aligned} \frac{\partial\phi_n}{\partial t} + \nabla\cdot(\phi_n\mathbf{v}_n) = g_n,\\ \frac{\partial\phi_s}{\partial t} + \nabla\cdot(\phi_s\mathbf{v}_s) = 0, \end{aligned} \tag{1.2}$$

and the equation for the nutrient substrate consumption is given by

$$\frac{\partial}{\partial t}(\phi_s c) + \nabla\cdot(c\mathbf{v}_s\phi_s - D_s\phi_s\nabla c) = -g_c, \tag{1.3}$$

where $g_n$ is the production rate for the polymer network, $g_c$ is the consumption rate of the nutrient substrate in the solvent, and $D_s$ is the diffusion constant of the nutrient substrate.

Both the polymer network and the solvent are assumed viscous in the Cogan–Keener model. The extra stress tensor, the osmotic pressure, and the production as well as consumption rates are given by the following constitutive laws:

$$\begin{aligned} \tau_n &= 2\eta_n\mathbf{D}_n,\\ \tau_s &= 2\eta_s\mathbf{D}_s,\\ g_c &= \phi_n A c,\\ g_n &= \epsilon\mu\phi_n\frac{c}{K_c+c},\\ \Psi &= \frac{kT}{v_1}\left[\ln(1-\phi_n) + \left(1-\frac{1}{N}\right)\phi_n + \chi\phi_n^2\right], \end{aligned} \tag{1.4}$$

where $\eta_{n,s}$ are the viscosity of the network and the solvent, respectively, $\mathbf{D}_{n,s} = \frac{1}{2}[\nabla_{n,s}+\nabla\mathbf{v}_{n,s}^T]$ is the rate of strain tensor for the network and the solvent, respectively, $A$ is the consumption rate of the substrate, $\mu$ is the maximum production rate, $K_c$ is the half-saturation constant and $\epsilon$ is a scaling parameter, $N$ is the polymerization index, $v_1$ is the volume of the solvent molecule, $k$ is the Boltzmann constant, $T$ is the temperature, and $\chi$ is the Flory–Huggins mixing parameter [15, 16]. We note that the equation for the concentration of bacteria is a decoupled equation in the Cogan–Keener model and is therefore not listed above.

Given that

$$\phi_n + \phi_s = 1, \tag{1.5}$$

the following constraints arise:

$$\begin{aligned} \nabla\cdot(\phi_n\mathbf{v}_n + \phi_s\mathbf{v}_s) &= g_n, \\ \nabla\cdot(\phi_n\tau_n + \phi_s\tau_s) &= \nabla(\Psi + p). \end{aligned} \tag{1.6}$$

We note that $\mathbf{v} = \phi_n\mathbf{v}_n + \phi_s\mathbf{v}_s$ is the volume averaged velocity. Clearly, it is not divergence-free when $g_n \neq 0$, indicating that the material is in fact "compressible." The second constraint gives the force balance equation for the volume averaged stress.

We note that the constraint above leads the bulk volume of the two-fluid material system to increase when $g_n \neq 0$. Practically, the individual velocity of each species is hardly measurable; moreover, it is impossible to impose the boundary conditions for ~~the~~ velocities at inflow and outflow boundaries for each species. Therefore two-fluid theories are not easy to adopt in fluid dynamics and rheological studies. The practical use of the two-fluid models includes ignoring the solvent velocity [7], ignoring the stress deformation [22], or simply imposing periodic boundary conditions. This clearly limits the applicability of the multifluid biofilm theories.

In this paper, we embark on a different approach, assuming the biofilm-solvent mixture is incompressible, whose bulk motion is measured by a divergence-free averaged velocity field, adopting the one-fluid multicomponent formulation for mixture theories [2]. We retain the effective treatment of the polymer network/bacteria and substrate/solvent combinations. The excessive velocity in addition to the average one is accounted for by ~~the~~ polymer-solvent mixing dynamics. Through an essentially mean field approach, we can couple the polymer network deformation and biofilm/solvent interfacial dynamics into the fluid mixture motion, which to the best of our knowledge has not been done to biofilm models systematically so far. The effective polymer comprising the EPS and bacteria is modeled as a viscoelastic "solution" in which the bacterium is the solution since it is viscous while the EPS is modeled as a linear polymer strand of a network [3].

The rest of this paper is organized as follows. First we develop a set of phase field models for biofilms by accounting for the transport of polymer networks, nutrient substrates, and the response of the polymer network in flow in several plausible ways within the theoretical framework of one-fluid multicomponent systems. We then analyze the stability of some steady states to investigate possibly unstable modes. Finally, we numerically study the biofilm growth and expansion in one space dimension and compare the results with respect to various formulations of the mixture theory.

**2. Mathematical models.** We study the biofilm in solvent as a fluid mixture of two components: The effective polymer network ~~includ~~ing the bacteria trapped inside and the effective solvent which includes the nutrient substrates and pure solvent. We

adopt the one-fluid two-component formalism for fluid mixtures to develop a single-fluid, multicomponent model using the volume averaged velocity and the volume fractions of the two distinctive components. The polymer network volume fraction $\phi_n$ plays the role of a phase field variable in the theory. When $\phi_n = 0$, the fluid consists of entirely the solvent; otherwise, it is a true binary mixture when $0 < \phi_n < 1$. (The case of $\phi_n = 1$ is excluded in biofilms since they are never dry.) Therefore, the resulting theory is an effective phase field model. The two distinctive phases are modeled by $\phi_n = 0$ and $\phi_n > 0$, respectively. The inhomogeneity of the biofilm is accounted for by the variation of $\phi_n$.

**2.1. Phase field formulation.** When the fluid mixture is incompressible, the average velocity is divergence-free. The bulk fluid is convected by the average velocity. In addition to the bulk convection, the polymer network is also transported by an additional flux due to ~~the~~ mixing of two different components. Specifically, the local instantaneous flux consists of two parts: The flux convected by the average velocity $\mathbf{v}$ and the excessive flux due to ~~the~~ polymer-solvent binary mixing. The later contribution to the flux of the polymer volume fraction is assumed proportional to the mixing force given by the gradient of the free energy variation

$$\mathbf{f}_n = -\lambda_{ch} \nabla \frac{\partial f}{\partial \phi_n}, \tag{2.1}$$

where $\lambda_{ch}$ is the proportionality parameter that has the same unit as the mobility. This is consistent with the Ginzburg–Landau dynamics in condensed matter physics [6]. The mixing free energy density $f$ as a function of $\phi_n$ is given by the extended Flory–Huggins free energy density [15, 16]

$$f = kT \left[ \frac{\gamma_1}{2} \|\nabla \phi_n\|^2 + \gamma_2 \left( \frac{\phi_n}{N} \ln \phi_n + (1-\phi_n) \ln(1-\phi_n) + \chi \phi_n (1-\phi_n) \right) \right], \tag{2.2}$$

where $\gamma_1$ and $\gamma_2$ measure the strength of the distortional and bulk mixing free energy, respectively, $\chi$ is the Flory–Huggins mixing parameter, $N$ is the generalized polymerization index, $1/\gamma_2$ is proportional to the specific volume of the solvent molecule, and $\|\cdot\|$ denotes the $l_2$ norm of a vector in $\mathbf{R}^3$. The distortional free energy is included in the extended Flory–Huggins mixing free energy to account for the surface tension effect at the solvent-biofilm interface defined by ~~$\phi_n = 0$~~ and penalizing spatial inhomogeneity in the mixture. The variation of $f$ with respect to $\phi_n$ (known as the chemical potential) is given by

$$\frac{\delta f}{\delta \phi_n} = -kT \left[ \gamma_1 \Delta \phi_n + \gamma_2 \left[ -\frac{1}{N} - \frac{\ln \phi_n}{N} + \ln(1-\phi_n) + 1 - \chi + 2\chi \phi_n \right] \right]. \tag{2.3}$$

Representing the growth rate of the polymer network produced by bacteria as the reaction rate for the polymer volume fraction, we propose the transport equation for the volume fraction of the polymer network as follows:

$$\frac{\partial \phi_n}{\partial t} + \nabla \cdot (\phi_n \mathbf{v}) = \nabla \cdot \left( \lambda_{ch} \nabla \frac{\delta f}{\delta \phi_n} \right) + g_n. \tag{2.4}$$

This is the Cahn–Hilliard equation [4, 5] with a reaction term (polymer production). From the given excessive flux, we can identify the instantaneous excessive velocity as

$$\mathbf{v}_n^e = -\lambda_{ch} \frac{1}{\phi_n} \nabla \frac{\delta f}{\delta \phi_n} \tag{2.5}$$

when $\phi_n \neq 0$. It is zero when $\phi_n = 0$.

Another form of the transport equation for $\phi_n$ can be obtained by arguing that the excessive flux is due to an excessive velocity which is proportional to the mixing force and takes the form $\mathbf{v}_n^e = -\lambda\nabla\frac{\delta f}{\delta\phi_n}$, in which the excessive flux is given by $-\lambda\phi_n\nabla\frac{\delta f}{\delta\phi_n}$. Here $\lambda$ is the mobility parameter. This can also be obtained from the Ginzburg–Landau dynamics by assuming that $\lambda_{ch}$ is proportional to the polymer volume fraction: $\lambda_{ch} = \lambda\phi_n$. The transport equation for $\phi_n$ is given by

$$\frac{\partial\phi_n}{\partial t} + \nabla\cdot(\phi_n\mathbf{v}) = \nabla\cdot\left[\lambda\phi_n\nabla\frac{\delta f}{\delta\phi_n}\right] + g_n. \tag{2.6}$$

This is called the modified or singular Cahn–Hilliard equation. When the fluid is entirely occupied by polymer networks, one of the extreme cases, we argue that ~~the~~ mixing will cease. Therefore, it is plausible to assume that the mobility matrix is proportional to the solvent volume fraction as well:

$$\lambda = \lambda_0(1-\phi_n). \tag{2.7}$$

However, this perhaps would never happen in biofilm materials since biofilms always contain solvent in their sponge-like structures. Both ~~of~~ the Cahn–Hilliard and the modified Cahn–Hilliard models will be tested in the following. The numerical simulation presented in later sections shows that the modified Cahn–Hilliard equation is more appropriate for the transport of $\phi_n$, especially with the polymer production included in the transport ~~equation~~.

The remaining governing equations for the mixture consist of the continuity equation, the momentum transport or balance equation, and the transport equation for the nutrient:

$$\begin{aligned}
&\nabla\cdot\mathbf{v} = 0,\\
&\rho\frac{d\mathbf{v}}{dt} = \nabla\cdot(\tau_{extra}) - [\nabla p + \gamma_1 kT\nabla\cdot(\nabla\phi_n\nabla\phi_n)],\\
&\frac{\partial}{\partial t}(\phi_s c) + \nabla\cdot(c\mathbf{v}\phi_s - D_s\phi_s\nabla c) = -g_c,
\end{aligned} \tag{2.8}$$

where $\rho_s$ and $\rho_n$ are the density of the solvent and polymer, respectively, $\rho = \phi_s\rho_s + \phi_n\rho_n$ is the averaged density, and $\tau_{extra}$ is the total extra bulk stress for the mixture. Here $g_n$, $g_c$ are the reaction rates defined in (1.4). We note that when the densities of the polymer network and solvent are equal, the density of the mixture is a constant and the volume fraction averaged velocity is the mass averaged velocity.

In the above momentum balance equation, the presence of the extra term $\gamma_1 kT\nabla\cdot(\nabla\phi_n\nabla\phi_n)$ is due to the spatial inhomogeneity resulting from a virtual work principle [24]. The nutrient transport is assumed to be convected by the average velocity. The incompressibility condition $\nabla\cdot\mathbf{v} = 0$ and the constraint $\phi_n + \phi_s = 1$ require that the transport equation for $\phi_s$ have a decay term $-g_n$, leading to

$$\frac{\partial\phi_s}{\partial t} + \nabla\cdot(\phi_s\mathbf{v}) = -\nabla\cdot\left(\lambda_{ch}\nabla\frac{\delta f}{\delta\phi_n}\right) - g_n \tag{2.9}$$

in the Cahn–Hilliard model or

$$\frac{\partial\phi_s}{\partial t} + \nabla\cdot(\phi_s\mathbf{v}) = -\nabla\cdot\lambda\left(\phi_n\nabla\frac{\delta f}{\delta\phi_n}\right) - g_n \tag{2.10}$$

in the modified Cahn–Hilliard model. In the Cahn–Hilliard model, the excessive solvent velocity can be identified as

$$\mathbf{v}_s^e = \lambda_{ch} \frac{1}{\phi_s} \nabla \frac{\delta f}{\delta \phi_n}, \tag{2.11}$$

whereas the velocity is given by

$$\mathbf{v}_s^e = \lambda \frac{\phi_n}{\phi_s} \nabla \frac{\delta f}{\delta \phi_n} \tag{2.12}$$

in the modified Cahn–Hilliard model. The actual solvent velocity can be calculated by

$$\mathbf{v}_s = \mathbf{v} + \mathbf{v}_s^e. \tag{2.13}$$

Analogously, the polymer network velocity is given by

$$\mathbf{v}_n = \mathbf{v} + \mathbf{v}_n^e. \tag{2.14}$$

With this definition, we easily see that the average velocity is indeed the volume averaged velocity

$$\mathbf{v} = \phi_n \mathbf{v}_n + \phi_s \mathbf{v}_s. \tag{2.15}$$

In the above formulation of the theory, the nutrient substrate is assumed to be transported along with the average velocity. If we assume that the nutrient is transported with the solvent velocity instead, the nutrient transport equation is given by

$$\frac{\partial}{\partial t}(\phi_s c) + \nabla \cdot (c \mathbf{v}_s \phi_s - D_s \phi_s \nabla c) = -g_c. \tag{2.16}$$

**2.2. Constitutive equations for effective polymer.** The extra stress for the polymer network–solvent mixture will supply the crucial link to complete the governing system of equations for the biofilm model. The simplest choice is treating the polymer-solvent mixture as an extended Newtonian fluid like in (2.17). When both the solvent and the polymer are modeled as viscous fluids, the constitutive equations for the extra stresses are given by

$$\tau_n = 2\eta_n \mathbf{D}, \qquad \tau_s = 2\eta_s \mathbf{D}, \tag{2.17}$$

where $\mathbf{D} = \frac{1}{2}[\nabla \mathbf{v} + \nabla \mathbf{v}^T]$ is the rate of strain tensor and $\eta_n$, $\eta_s$ are the polymer and solvent viscosities, respectively. Alternatively, we assume the extra stress to be proportional to the rate of strain tensor given by the velocity field of each component:

$$\tau_n = 2\eta_n \mathbf{D}_n, \qquad \tau_s = 2\eta_s \mathbf{D}_s, \tag{2.18}$$

where $\mathbf{D}_n = \frac{1}{2}(\nabla \mathbf{v}_n + \nabla \mathbf{v}_n^T)$, $\mathbf{D}_s = \frac{1}{2}(\nabla \mathbf{v}_s + \nabla \mathbf{v}_s^T)$. To account for the shear thinning effect, the polymer viscosity could depend on the rate of strain tensor like the power-law type [3].

However, because biofilms are hydrogels, they exhibit elastic and/or viscoelastic behavior depending on the time-scale of interest. To account for these contributions of the network, more sophisticated constitutive equations should be employed. We

propose both an elastic and a viscoelastic model next. Given the composition of the effective polymer network, the stress associated to it should contains a viscous part accounting for the stress due to the viscous bacterial component denoted by $\tau_{ns}$. It has two variations

$$\tau_{ns} = 2\eta_n \mathbf{D} \quad \text{or} \quad \tau_{ns} = 2\eta_n \mathbf{D}_n \tag{2.19}$$

Here, $\eta_n$ is the bacterial contribution to the polymeric viscosity due to the presence of bacteria in the effective polymer.

*Rubber-elastic model.* We model the EPS network as a gel. According to rubber-elastic theory, the elastic constitutive equation is given by

$$\tau_n = \nu kT \mathbf{F} \cdot \mathbf{F}^T = \nu kT \mathbf{B}, \tag{2.20}$$

where $\mathbf{F}$ is the deformation gradient tensor, $\mathbf{B} = \mathbf{F} \cdot \mathbf{F^T}$ is the Finger tensor, and $\nu$ is the polymer number density. The time evolution of the deformation gradient tensor in the absence of solvent is given by

$$\frac{d\mathbf{F}}{dt} = \nabla \mathbf{v}_n \cdot \mathbf{F}, \tag{2.21}$$

where $\mathbf{v}_n$ is the polymer network velocity. The time evolution of the elastic stress tensor (as well as Finger tensor B) follows the equation

$$\frac{\partial \tau_n}{\partial t} + \mathbf{v}_n \cdot \nabla(\tau_n) - [\nabla \mathbf{v}_n \cdot \tau_n + \tau_n \cdot \nabla \mathbf{v}_n^T] = 0. \tag{2.22}$$

An alternative choice for the rate-of-strain tensor is the rate of strain associated with the average velocity. Then, the constitutive equation for the elastic stress tensor is given by

$$\frac{d\tau_n}{dt} - [\nabla \mathbf{v} \cdot \tau_n + \tau_n \cdot \nabla \mathbf{v}^T] = 0, \tag{2.23}$$

where $\frac{d}{dt}(\bullet) = \frac{\partial}{\partial t}(\bullet) + \mathbf{v} \cdot \nabla(\bullet)$ is the material derivative and the polymer network is assumed to deform with the average velocity gradient.

*Johnson–Segalman model.* Considering the creation and annihilation rate for the network strands or segments in the network, we adopt the temporary network model for the viscoelastic EPS [3]. When the two rates are balanced, the constitutive equation for the elastic stress tensor is given by the following Johnson–Segalman model:

$$\frac{\partial \tau_n}{\partial t} + \mathbf{v}_n \cdot \nabla \tau_n - \mathbf{W}_n \cdot \tau_n + \tau_n \cdot \mathbf{W}_n - a[\mathbf{D}_n \cdot \tau_n + \tau_n \cdot \mathbf{D}_n] + \frac{\tau_n}{\lambda_1} = \frac{2\eta_p}{\lambda_1} \mathbf{D}_n, \tag{2.24}$$

where $a$ is a rate parameter between $-1$ and 1, $\lambda_1$ is the relaxation time, and $\eta_p$ is the EPS polymer network viscosity in the effective polymer [3]. $a = 1$ yields the Oldroyd-B model with the upper convected derivative, and $a = -1$ corresponds to the lower convected derivative. The rubber-elastic model can be viewed as a limiting case of the current model as $\lambda_1 \to \infty$ and $a = 1$; the viscous limit is recovered if $\lambda_1 \to 0$; whereas the highly elastic model is the limit of $\lambda_1 \to \infty$, $\frac{\eta_p}{\lambda_1} \to G$, where $G$ is the elastic modulus.

An alternative formulation is to replace the network velocity $\mathbf{v}_n$ by the average velocity $\mathbf{v}$ analogous to the rubber-elastic case. The constitutive equation for the extra stress is then given by

$$\frac{\partial \tau_n}{\partial t} - \mathbf{W}\cdot\tau_n + \tau_n\cdot\mathbf{W} - a[\mathbf{D}\cdot\tau_n + \tau_n\cdot\mathbf{D}] + \frac{\tau_n}{\lambda_1} = \frac{2\eta_p}{\lambda_1}\mathbf{D}. \tag{2.25}$$

In summary, the phase field theories for biofilms consist of four sets of equations of multiple variations. In the following, the suffix A indicates that the average velocity is used, while N denotes that the network and the solvent velocity, respectively, are used.

*Momentum and continuity equation.*

$$\begin{aligned} \nabla\cdot\mathbf{v} &= 0,\\ \rho\frac{d\mathbf{v}}{dt} &= \nabla\cdot(\tau_{extra}) - [\nabla p + \gamma_1 kT\nabla\cdot(\nabla\phi_n\nabla\phi_n)],\\ \tau_{extra} &= \phi_n(a\tau_n + \tau_{ns}) + \phi_s\tau_s. \end{aligned} \tag{2.26}$$

*Transport equation for nutrients.*

$$\begin{aligned} &\frac{\partial}{\partial t}(\phi_s c) + \nabla\cdot(c\mathbf{v}\phi_s - D_s\phi_s\nabla c) = -g_c, \qquad \text{(CA-model)}\\ &\frac{\partial}{\partial t}(\phi_s c) + \nabla\cdot(c\mathbf{v}_s\phi_s - D_s\phi_s\nabla c) = -g_c. \qquad \text{(CN-model)} \end{aligned} \tag{2.27}$$

*Transport equation for the polymer network volume fraction.*

$$\begin{aligned} &\frac{\partial\phi_n}{\partial t} + \nabla\cdot(\phi_n\mathbf{v}) = \nabla\cdot\left[\lambda_{ch}\nabla\frac{\delta f}{\delta\phi_n}\right] + g_n, \qquad \text{(CH-model)}\\ &\frac{\partial\phi_n}{\partial t} + \nabla\cdot(\phi_n\mathbf{v}) = \nabla\cdot\left[\lambda\phi_n\nabla\frac{\delta f}{\delta\phi_n}\right] + g_n. \qquad \text{(MCH-model)} \end{aligned} \tag{2.28}$$

*Constitutive equations.*

$$\begin{gathered} \tau_n = 2\eta_n\mathbf{D},\ \tau_{ns} = 0,\ \tau_s = 2\eta_s\mathbf{D},\ a = 1, \qquad \text{(VA-model)}\\ \tau_n = 2\eta_n\mathbf{D}_n,\ \tau_{ns} = 0,\ \tau_s = 2\eta_s\mathbf{D}_s,\ a = 1, \qquad \text{(VN-model)}\\ \frac{d\tau_n}{dt} - \mathbf{W}\cdot\tau_n + \tau_n\cdot\mathbf{W} - a[\mathbf{D}\cdot\tau_n + \tau_n\cdot\mathbf{D}] + \frac{\tau_n}{\lambda_1} = \frac{2\eta_p}{\lambda_1}\mathbf{D},\\ \tau_{ns} = 2\eta_n\mathbf{D},\ \tau_s = 2\eta_s\mathbf{D}, \qquad \text{(JSA-model)}\\ \frac{\partial\tau_n}{\partial t} + \nabla\cdot(\mathbf{v}_n\tau_n) - \mathbf{W}_n\cdot\tau_n + \tau_n\cdot\mathbf{W}_n - a[\mathbf{D}_n\cdot\tau_n + \tau_n\cdot\mathbf{D}_n] + \frac{\tau_n}{\lambda_1} = \frac{2\eta_p}{\lambda_1}\mathbf{D}_n,\\ \tau_{ns} = 2\eta_n\mathbf{D}_n,\ \tau_s = 2\eta_s\mathbf{D}_s. \qquad \text{(JSN-model)} \end{gathered} \tag{2.29}$$

The production rate for polymer network and the consumption rate for the nutrient follow those of the Cogan–Keener model defined in section 1. In the MCH model, the mobility parameter $\lambda$ can also be assigned to $\lambda_0\phi_s$ in case the solvent volume fraction is low and varies drastically in space.

**3. Nondimensionalization.** We use a characteristic time-scale $t_0$ and length-scale $h$, whose values will be specified in specific applications, to nondimensionalize the variables

$$\tilde{t} = \frac{t}{t_o},\quad \tilde{\mathbf{x}} = \frac{\mathbf{x}}{h},\quad \tilde{\mathbf{v}} = \frac{\mathbf{v}t_0}{h},\quad \tilde{p} = \frac{pt_0^2}{\rho_0 h^2},\quad \tilde{\tau}_n = \frac{\tau_n t_0^2}{\rho_0 h^2},\quad \tilde{c} = \frac{c}{c_0}, \tag{3.1}$$

where $c_0$ is a characteristic substrate concentration.The following dimensionless quantities arise:

(3.2)
$$\Lambda = \frac{\lambda\rho_0}{t_0},\ \Gamma_1 = \frac{\gamma_1 kTt_0^2}{\rho_0 h^4},\ \Gamma_2 = \frac{\gamma_2 kTt_0^2}{\rho_0 h^2},\ Re_s = \frac{\rho_0 h^2}{\eta_s t_0},\ Re_n = \frac{\rho_0 h^2}{\eta_n t_0},\ Re_p = \frac{\rho_0 h^2}{\eta_p t_0},$$
$$\tilde{D}_s = \frac{D_s t_0}{h^2},\ \Lambda_1 = \frac{\lambda_1}{t_0},\ \tilde{\rho} = \phi_s\frac{\rho_s}{\rho_0} + \phi_n\frac{\rho_n}{\rho_0}, \tilde{A} = At_0,\ \tilde{\mu} = \mu t_0,\ \tilde{K}_c = \frac{K_c}{c_0},$$

where $\rho_0$ is an averaged density; $Re_{s,n,p}$ are the Reynolds numbers for the solvent, bacteria in the effective polymer network, and EPS polymer network; $\Lambda_1$ is the Deborah number for the polymer network; $\lambda$, $\Gamma_{1,2}$, $\tilde{D}_s$, $\tilde{A}$, $\tilde{\mu}$, $\tilde{K}_c$ are the dimensionless parameters of the dimensional counterparts. For simplicity, we drop $\tilde{\bullet}$ on the dimensionless variables, and the parameters and the system of governing equations in these dimensionless variables are given, for example in the CH+CA+JSA model, by

$$\begin{aligned}
&\nabla\cdot\mathbf{v} = 0,\\
&\rho\frac{d\mathbf{v}}{dt} = \nabla\cdot(\phi_n(a\tau_n + \tau_{ns}) + \phi_s\tau_s) - [\nabla p + \Gamma_1\nabla\cdot(\nabla\phi_n\nabla\phi_n)],\\
&\frac{\partial}{\partial t}(\phi_s c) + \nabla\cdot(c\mathbf{v}\phi_s - D_s\phi_s\nabla c) = -g_c, \quad \text{(CA)}\\
&\frac{\partial\phi_n}{\partial t} + \nabla\cdot(\phi_n\mathbf{v}) = \nabla\cdot\left[\Lambda\nabla\frac{\delta f}{\delta\phi_n}\right] + gn, \quad \text{(CH)}\\
&\frac{d\tau_n}{dt} - \mathbf{W}\cdot\tau_n + \tau_n\cdot\mathbf{W} - a[\mathbf{D}\cdot\tau_n\tau_n\cdot\mathbf{D}] + \frac{\tau_n}{\Lambda_1} = \frac{2}{\Lambda_1 Re_p}\mathbf{D},\\
&\tau_{ns} = \frac{2}{Re_n}\mathbf{D}, \quad \tau_s = \frac{2}{Re_s}\mathbf{D}, \quad g_c = A\phi_n c, \quad gn = \epsilon\mu\phi_n\frac{c}{K_c + c}.
\end{aligned} \tag{3.3}$$

The mixing free energy density is now given by

$$f = \frac{\Gamma_1}{2}\|\nabla\phi_n\|^2 + \Gamma_2\left[\frac{\phi_n}{N}\ln\phi_n + (1-\phi_n)\ln(1-\phi_n) + \chi\phi_n(1-\phi_n)\right]. \tag{3.4}$$

The other dimensionless equations can be obtained analogously. To save space, we will not enumerate them here.

**4. Steady states in one dimension and their linear stability.** In this section we examine the solution of the governing system of equations that depend on one spatial variable $y \in I = [0,1]$, where the characteristic length-scale $h$ is chosen as the width of the stripe which the fluid mixture occupies. The boundary conditions for the governing system of equations are

$$\mathbf{v}|_{\partial I} = \mathbf{v}^0, \quad \left[\phi_n\mathbf{n}\cdot\nabla\frac{\delta f}{\delta\phi_n}\right]_{\partial I} = 0, \quad [\mathbf{n}\cdot\nabla\phi_n]_{\partial I} = 0, \quad [\phi_s\mathbf{n}\cdot\nabla c]_{\partial I} = 0, \tag{4.1}$$

where $\mathbf{n}$ is the unit external normal at the boundary of the domain $I$ and $\partial I$ denotes the boundary of the domain. These boundary conditions consist of the no-slip boundary condition on the solid boundary for the average velocity as well as the excessive polymer network velocity, and a no-flux boundary condition for the polymer network volume fraction and for the nutrient concentration.

**4.1. Viscous limit.** We first discuss the solution given by the viscous model (CH+VA) ~~denoted~~ $\eta_m = \frac{1-\phi_n}{Re_s} + \frac{\phi_n}{Re_n}$, where $1/\eta_m$ is the effective Reynolds number and

$$\hat{f}(\phi_n) = \frac{\phi_n}{N}\ln\phi_n + (1-\phi_n)\ln(1-\phi_n) + \chi\phi_n(1-\phi_n), \tag{4.2}$$

is the bulk Flory–Huggin mixing free energy density. Considering the boundary condition at the wall, we set $v_y^0 = 0$.

The constant steady state solution for all models is given by

$$\begin{aligned} &\mathbf{v} = \mathbf{0}, \quad p = p_0, \quad \phi_n = \phi_0, \quad c = 0, \text{ or} \\ &\mathbf{v} = \mathbf{0}, \quad p = p_0, \quad \phi_n = 0, \quad c = c_0, \end{aligned} \tag{4.3}$$

where $p_0$ is an arbitrary constant, $c_0$ is an arbitrary positive constant, and $0 \le \phi_0 < 1$ is a constant. In addition to the constant solutions, there can exist a nonconstant steady state at $c = 0$ for $\phi_n$ ~~given~~ by

$$\Gamma_1\phi_n'' - \Gamma_2\frac{\partial\hat{f}}{\partial\phi_n} = \Gamma_1 C_0. \tag{4.4}$$

A closed form of the solution is not available for this equation. However, (4.4) can be integrated to yield

$$\phi_n' = \pm\sqrt{2C_0\phi_n + \frac{2\Gamma_2}{\Gamma_1}\hat{f}(\phi_n) + 2C_1}, \tag{4.5}$$

where $C_0$ and $C_1$ are integrating constants. A qualitative phase space analysis on an analogous system is given in [22]. Here we focus on the nonconstant steady state satisfying the Neumann boundary condition.

Using the boundary condition $\phi_n'(1) = \phi_n'(0) = 0$, we can determine $C_0$ and $C_1$:

$$\begin{aligned} 2C_0\phi_n(1) + \frac{2\Gamma_2}{\Gamma_1}\hat{f}(\phi_n(1)) + 2C_1 = 0, \\ 2C_0\phi_n(0) + \frac{2\Gamma_2}{\Gamma_1}\hat{f}(\phi_n(0)) + 2C_1 = 0. \end{aligned} \tag{4.6}$$

If $\phi_n(0) \neq \phi_n(1)$,

(4.7)
$$C_0 = \frac{\Gamma_2}{\Gamma_1}\,\frac{\hat{f}(\phi_n(0)) - \hat{f}(\phi_n(1))}{\phi_n(1) - \phi_n(0)}, \qquad C_1 = -\frac{\Gamma_2}{\Gamma_1}\,\frac{\phi_n(1)\hat{f}(\phi_n(0)) - \phi_n(0)\hat{f}(\phi_n(1))}{\phi_n(1) - \phi_n(0)}.$$

If we denote

$$g(\phi) = -\frac{\Gamma_1}{\Gamma_2}[C_0\phi_n + C_1], \tag{4.8}$$

$g(\phi)$ is the secant-line interpolating ~~between~~ the points $(\phi_n(0), \hat{f}(\phi_n(0)))$ and $(\phi_n(1), \hat{f}(\phi_n(1)))$. In order to have a smooth real solution, $\hat{f} - g > 0$; i.e., $\hat{f}$ is concave down between $\phi_n(0)$ and $\phi_n(1)$ The concavity region of $\hat{f}$ is depicted in Figure 1 in phase space $(\phi, \chi)$ at $N = 1000$. In the concave down region, a smooth solution can exist depending on the magnitude of $\frac{2\Gamma_2}{\Gamma_1}$.

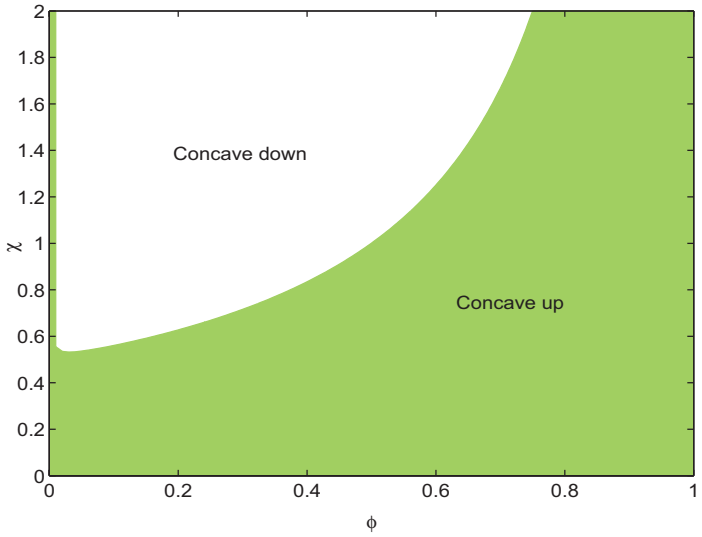


FIG. 1. *The regions of concavity in phase space* $(\phi, \chi)$ *at* $N = 1000$.

From (4.5), we can see that the steady state solution is either monotonically increasing or decreasing if it exists. Integrating (4.5), we arrive at

$$\pm \int_{\phi_n(0)}^{\phi_n(y)} \frac{d\phi}{\sqrt{\hat{f}(\phi) - g(\phi)}} = y\sqrt{\frac{2\Gamma_2}{\Gamma_1}}, \tag{4.9}$$

where the solution of the boundary value problem is constrained by

$$\pm \int_{\phi_n(0)}^{\phi_n(1)} \frac{d\phi}{\sqrt{\hat{f}(\phi) - g(\phi)}} = \sqrt{\frac{2\Gamma_2}{\Gamma_1}}. \tag{4.10}$$

Notice that $\frac{2\Gamma_2}{\Gamma_1} = \frac{2h^2\gamma_2}{\gamma_1}$. Unless this dimensionless quantity is small, there could not be a solution to the integral equation. When the right-hand side is small, the chance to have a smooth solution increases considerably.

If $\phi_n(0) = \phi_n(1)$, we can determine $C_0$ only in terms of $C_1$:

$$C_1 = -C_0\phi_n(1) - \frac{\Gamma_2}{\Gamma_1}\hat{f}(\phi_n(1)). \tag{4.11}$$

The governing equation is given by

$$\phi_n' = \pm\sqrt{\frac{2\Gamma_2}{\Gamma_1}\left[\hat{f}(\phi_n) - \left(-\frac{C_0\Gamma_1}{\Gamma_2}(\phi_n - \phi_n(0)) + \hat{f}(\phi_n(0))\right)\right]}. \tag{4.12}$$

The constant solution $\phi_n = \phi_n(0)$ is a solution. When $\hat{f}$ is concave down, there could be a nonconstant steady state given below, provided that $\frac{2h^2\gamma_2}{\gamma_1}$ is small:

(4.13)
$$\int_{\phi_n(0)}^{\phi_n(y)} \frac{d\phi}{\sqrt{\left[\hat{f}(\phi_n) - \left(-\frac{C_0\Gamma_1}{\Gamma_2}(\phi_n - \phi_n(0)) + \hat{f}(\phi_n(0))\right)\right]}} = y\sqrt{\frac{2\Gamma_2}{\Gamma_1}}, \quad 0 \le y \le \frac{1}{2},$$
$$\int_{\phi_n(1/2)}^{\phi_n(y)} \frac{d\phi}{\sqrt{\left[\hat{f}(\phi_n) - \left(-\frac{C_0\Gamma_1}{\Gamma_2}(\phi_n - \phi_n(0)) + \hat{f}(\phi_n(0))\right)\right]}} = -y\sqrt{\frac{2\Gamma_2}{\Gamma_1}}, \quad \frac{1}{2} < y \le 1,$$

or

(4.14)
$$\int_{\phi_n(0)}^{\phi_n(y)} \frac{d\phi}{\sqrt{\left[\hat{f}(\phi_n) - \left(-\frac{C_0\Gamma_1}{\Gamma_2}(\phi_n - \phi_n(0)) + \hat{f}(\phi_n(0))\right)\right]}} = -y\sqrt{\frac{2\Gamma_2}{\Gamma_1}}, \quad 0 \le y \le \frac{1}{2},$$
$$\int_{\phi_n(1/2)}^{\phi_n(y)} \frac{d\phi}{\sqrt{\left[\hat{f}(\phi_n) - \left(-\frac{C_0\Gamma_1}{\Gamma_2}(\phi_n - \phi_n(0)) + \hat{f}(\phi_n(0))\right)\right]}} = y\sqrt{\frac{2\Gamma_2}{\Gamma_1}}, \quad \frac{1}{2} < y \le 1.$$

This solution is spatially periodic with period 1.

Next, we examine the linearized stability of the constant states. Let $\rho^0 = \rho(\phi_0)$ be the averaged density at the steady state. The eigenfunction for the velocity components is $\sin(\beta y)$ and for $c$ and $\phi_n$ is $\cos(\beta y)$, respectively, where $\beta = m\pi$, $m = 1, \ldots, \infty$. The growth-rates of the linearized system are given by

(4.15)
$$\begin{aligned}
\alpha_{1,2} &= -\frac{1}{\rho^0}\left(\frac{1-\phi_0}{Re_s} + \frac{\phi_0}{Re_n}\right)\beta^2, \\
\alpha_3 &= \Lambda\left(-\Gamma_2\frac{\partial^2\hat{f}}{\partial\phi^2}(\phi_0)\beta^2 - \Gamma_1\beta^4\right), \\
\alpha_4 &= -D_n\beta^2 - A\phi_0,
\end{aligned}$$

where $\alpha_{1,2}$ are the growth-rates obtained from the linearized momentum equations, $\alpha_3$ is the growth-rate corresponding to the linearized transport equation for $\phi_n$, and $\alpha_4$ is the growth-rate for the nutrient concentration. If $\frac{\partial^2\hat{f}}{\partial\phi^2}(\phi_0) \ge 0$, i.e., the bulk mixing energy density curve is concave up, all the growth-rates are nonpositive; in fact, they are decay rates. Otherwise, in the portion where the mixing energy density is concave down, $\alpha_3$ is positive for small values of $\beta$ and negative for large values of $\beta$, ~~in which~~ the steady state suffers the long wave instability. We note that $\frac{\partial^2\hat{f}}{\partial\phi_n^2} = \frac{1}{N\phi_n} + \frac{1}{1-\phi_n} - 2\chi$, and thus $\frac{\partial^2\hat{f}}{\partial\phi_n^2} = 0$ has two solutions $\phi_n^{\pm}$. If $\phi_n^{\pm}$ are real, $\frac{\partial^2\hat{f}}{\partial\phi_n^2} < 0$ and $\hat{f}$ is concave down for $\phi_n^- < \phi_n < \phi_n^+$. The instability occurs in the concave down region. Figure 2 depicts $\hat{f}$ and $\frac{\partial^2\hat{f}}{\partial\phi_n^2}$ at $N = 10^3$ and two different values of $\chi$. In (c) and (d), the intersections of the dashed line with the curve give values of $\phi_n^{\pm}$. It can be seen for larger values of $\chi$ that the range of $\phi_n$ where $\frac{\partial^2\hat{f}}{\partial\phi^2 n} < 0$ becomes wider.

For the second family of constant steady states (4.3.2) the eigen~~values~~ for the velocity, the nutrient sub-strate concentration, and the polymer network volume fraction are identical to the previous case ~~and given by $\sin(\beta y)$ and $\cos(\beta y)$, respectively~~. The growth-rates of the linearized system are given by

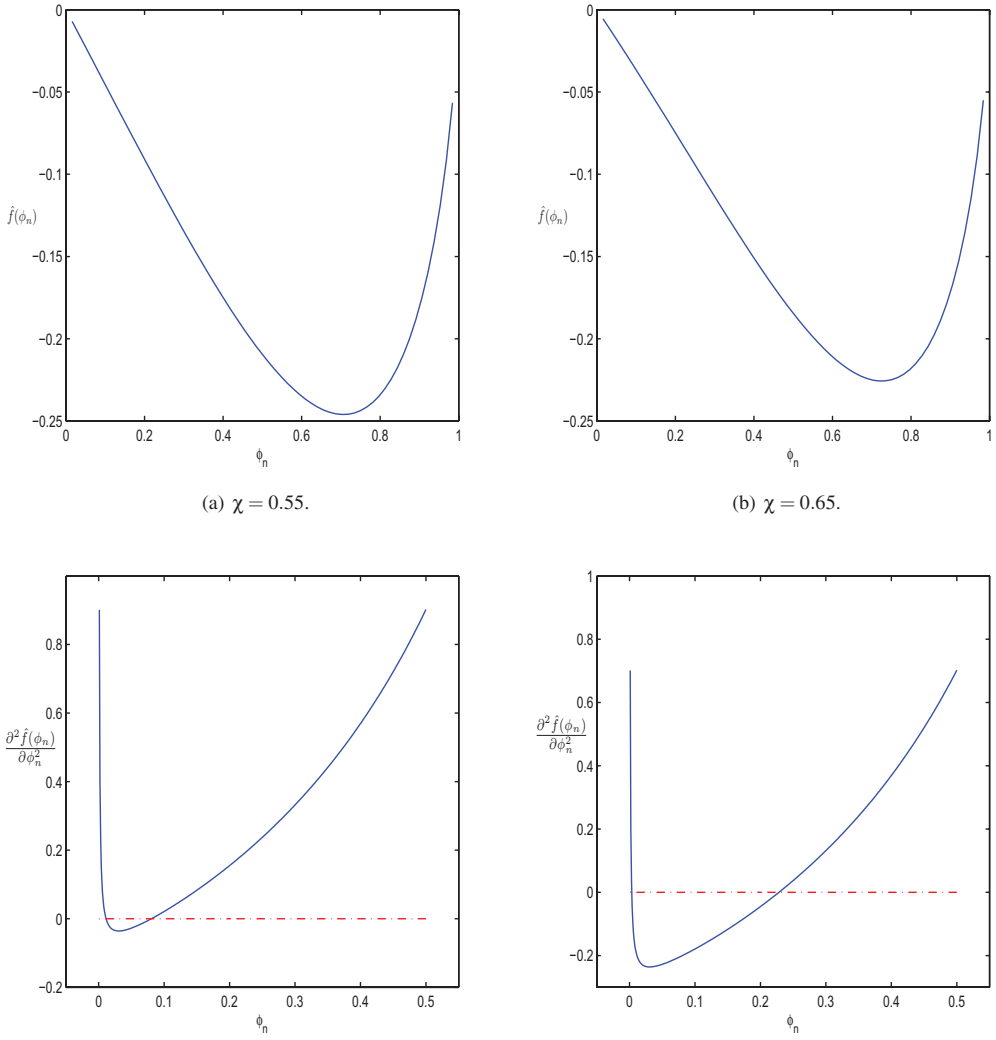


(a) $\chi = 0.55$. (b) $\chi = 0.65$.

(c) $\chi = 0.55$. (d) $\chi = 0.65$.

FIG. 2. *The normalized bulk mixing energy density* $\hat{f}(\phi_n)$ *and its second derivatives* $\frac{\partial^2 \hat{f}}{\partial \phi_n^2}$ *at* $\chi = 0.55, 0.65$. *At* $\chi = 0.55$, *the concave down region does not include* $\phi_n = 0.19$, *whereas it does at* $\chi = 0.65$.

(4.16)
$$\alpha_{1,2} = -\frac{1}{\rho^0 Re_s}\beta^2, \quad \alpha_3 = \Lambda\left(-\Gamma_2 \frac{\partial^2 \hat{f}}{\partial \phi^2}(0)\beta^2 - \Gamma_1 \beta^4\right) + \frac{\epsilon\mu c_0}{K + c_0}, \quad \alpha_4 = -D_s\beta^2.$$

We note that $\frac{\partial^2 \hat{f}}{\partial \phi_n^2}(0)$ is not defined in the original definition of the Flory–Huggin mixing free energy density. However, if we modify the $\phi_n \ln \phi_n$ term in the mixing energy density $f$ by $(\phi_n + \delta\phi)\ln(\phi_n + \delta\phi)$, where $0 < \delta\phi \ll 1$, then we have

$$\frac{\partial^2 \hat{f}}{\partial \phi_n^2} = \frac{1}{N(\phi_n + \delta\phi)} + \frac{1}{1 - \phi_n} - 2\chi,$$

and $\frac{\partial^2 \hat{f}}{\partial \phi_n^2}(0) = \frac{1}{N\delta\phi} + 1 - 2\chi$. If $\delta\phi \leq \frac{1}{N}$ and $0 \leq \chi \leq 1$, then $\frac{\partial^2 \hat{f}}{\partial \phi_n^2}(0) \geq 0$ and the only positive growth-rate comes from the polymer network production term at small $\beta$. For practical purposes, we use $\delta\phi = 10^{-6}$ throughout this paper.

We remark that the linearized stability analysis applies to the equations in an infinite domain and higher space dimensions as well. In this case, $\beta = \mathbf{k} \cdot \mathbf{l}$, where $\mathbf{k}$ is the wave number, $\mathbf{l}$ is a fixed direction in the multidimensional space, and the eigenfunctions are the Fourier (normal) modes. The analysis also applies to the three-dimensional cubic domain with homogeneous or periodic boundary conditions.

Figure 3 depicts the growth rates for the two families of constant steady states with dimensionless parameters $\Lambda = 10^{-9}$, $\Gamma_1 = 41.8337$, $\Gamma_2 = 418337$, $N = 10^3$, $\epsilon = 0$ and two selected values of $\chi$ at $\phi_n = 0.19$. For the first family of constant steady states, when $\chi = 0.55$, Figure 2(c) shows $\frac{\partial^2 \hat{f}}{\partial \phi_n^2}(0.19) > 0$, and thus the growth rate $\alpha_3 < 0$ for all $\beta > 0$; when $\chi = 0.65$, Figure 2(d) shows $\frac{\partial^2 \hat{f}}{\partial \phi_n^2}(0.19) < 0$, and thus $\alpha_3 > 0$ for $\beta$ between 0 and approximately 24. For the second family of constant steady states, a long wave instability persists to the infinitely long wave limit at any $\chi$. Numerical results confirming the long wave instability in nonlinear regimes are presented in section 6.

For the MCH model, the growth rate $\alpha_3$ is simply modified by a factor of $\phi_0$ for the first family of constant steady states

$$\alpha_3 = \phi_0 \Lambda \left( -\Gamma_2 \frac{\partial^2 \hat{f}}{\partial \phi^2}(\phi_0)\beta^2 - \Gamma_1 \beta^4 \right), \tag{4.17}$$

whereas ~~that~~ given by

$$\alpha_3 = \frac{\epsilon \mu c_0}{K_c + c_0} \tag{4.18}$$

for the second family of constant steady states, which equals the infinitely long wave limit of ~~that for the first steady state family~~.

We next examine the steady states and their stability in the viscoelastic models.

**4.2. Viscoelastic model.** The viscoelastic model adds a set of constitutive equations for the elastic stress to the governing system of equations and couples the elastic stress to the momentum transport equation. For brevity, we use $\tau$ in place of $\tau_n$ from here on for the polymer elastic stress tensor.

The steady state of the elastic stress tensor is zero. ~~The~~ constitutive equation for the polymer network stress is independent of the volume fraction $\phi_n$ and concentration $c$. ~~Given~~ the zero boundary conditions on $\mathbf{v}$, it is not necessary to impose any boundary conditions on the polymer elastic stress components. ~~Four~~ modes in the linearized constitutive equation are independent, and their growth rates are given by

$$\alpha_{5,7,8,10} = -\frac{1}{\Lambda_1}, \tag{4.19}$$

where the indices tracks the four decoupled modes of the elastic stress tensor. The other two modes $\alpha_{6,9}$ are coupled to the momentum equation. For the first family of steady states $\phi = \phi_0$, $c = 0$, the coupled growth rates are calculated as

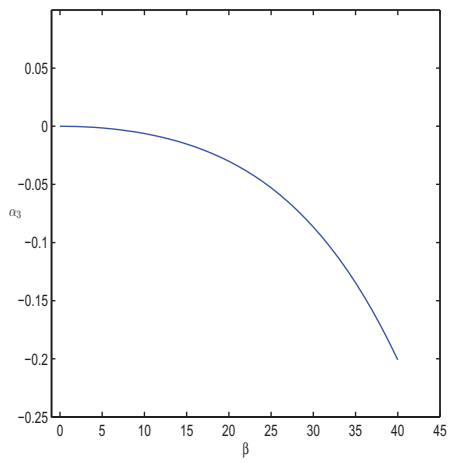


(a) Steady state 1, $\phi_n = \phi_0 = 0.19, c = 0$, and $\chi = 0.55$.

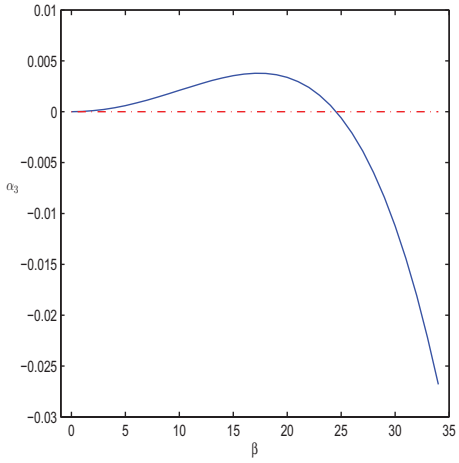


(b) Steady state 1, $\phi_n = \phi_0 = 0.19, c = 0$, and $\chi = 0.65$.

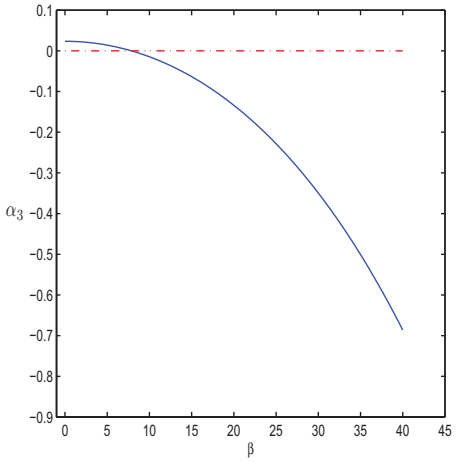


(c) Steady state 2, $\phi_n = 0, c = c_0$, and $\chi = 0.55$.

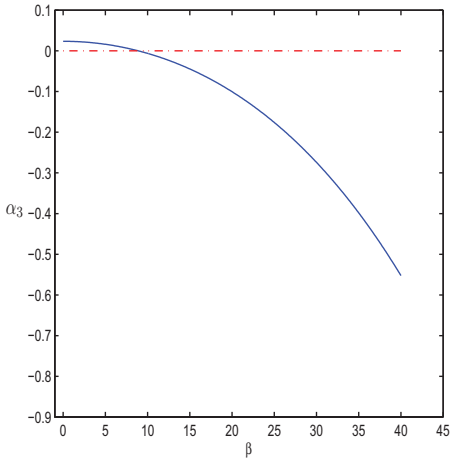


(d) Steady state 2, $\phi_n = 0, c = c_0$, and $\chi = 0.65$.

FIG. 3. *Growth rate of the linearized CH model. The values of the dimensionless parameters are* $\Lambda = 10^{-9}$, $\Gamma_1 = 41.8337$, $\Gamma_2 = 418337$, $N = 10^3$, $\delta\phi = 10^{-3}$, $\epsilon = 1$, $c_0 = 0.1$, $\mu = 0.14$, $K_c = 0.5$. *For the first family of steady states, the long wave growth is due to the polymer-solvent mixing kinetics shown in* (b). *Panel* (a) *depicts a negative growth rate. In contrast, for the second family of steady states, the long wave growth rate depends only on the polymer production shown in* (c) *and* (d).

(4.20)
$$\alpha_{1,2,6,9} = \frac{1}{2\rho_0}\left[-\left(\frac{\rho_0}{\Lambda_1} + \left(\frac{1-\phi_0}{Re_s} + \frac{\phi_0}{Re_n}\right)\beta^2\right) \pm \sqrt{\left(\frac{\rho_0}{\Lambda_1} + \frac{1-\phi_0}{Re_s}\beta^2\right)^2 - 4\rho_0\left(\left(\frac{1-\phi_0}{\Lambda_1 Re_s} + \frac{\phi_0}{\Lambda_1 Re_n}\right) + \frac{2a\phi_0}{\Lambda_1 Re_p}\beta^2\right)}\right].$$

The rates all have negative real parts. The corresponding eigenfunction for the velocity

components is $\sin \beta y$, and that for the stress components is $\cos \beta y$. The growth rates $\alpha_{3,4}$ and eigenfunctions for $\phi_n$ and $c$ are identical to those in the viscous limit.

For the second family of steady states $\phi = 0$, $c = c_0$. The linearized momentum and constitutive equations decouple. So, the growth-rates $\alpha_{1,2}$ remain in addition to the decay rates from the constitutive equations,

$$\alpha_{5,6,7,8,9,10} = -\frac{1}{\Lambda_1}. \tag{4.21}$$

In the gel model ($\Lambda_1 \to \infty$), the growth-rates are given by

$$\begin{aligned} \alpha_{1,2} &= -\left(\frac{1-\phi_0}{Re_s} + \frac{\phi_0}{Re_n}\right)\beta^2, \\ \alpha_{5,6,7,8,9,10} &= 0. \end{aligned} \tag{4.22}$$

The results for the JSN model are qualitatively the same and are omitted here. The analysis shows that the viscoelasticity at the linear regime does not have any negative effects on the stability. We next study the nonlinear dynamics of the biofilm flows in one space dimension. But first we present the numerical method that we use to compute the nonlinear transient solutions.

**5. Numerical scheme for the one-dimensional biofilm models.** In this section we investigate the growth of the biofilm in one dimension: $y \in I = [0, 1]$ governed by the momentum, Cahn–Hilliard ~~and~~ modified Cahn–Hilliard equations, the nutrient transport equation, and the stress constitutive equation JSA or JSN with the continuous supply of nutrient substrates through the top boundary. We adopt the boundary conditions given in (4.1) except that the nutrient boundary conditions are replaced by

$$[D\phi_s \nabla_y c] \cdot \mathbf{n}|_{y=0} = 0, \qquad c|_{y=1} = c^\star, \tag{5.1}$$

where $\mathbf{n}$ is the unit outward normal of $I$. The boundary condition on $c$ at $y = 1$ is the Dirichlet one, $c|_{y=1}$ $c^\star$, indicating that the substrate is fed at the top boundary to maintain a constant level of $c = c^\star$. The boundary condition for the velocity is chosen to be $\mathbf{v}_0|_{y=0} = (0, 0, 0)^T$, $\mathbf{v}_0|_{y=1} = (10^{-3}, 0, 0)^T$. We note that the vanishing boundary condition for $v_y$ along with the continuity condition warrants a vanishing velocity component in the $y$ direction. Thus the transport of the polymer network is entirely due to the excessive flux.

The numerical scheme used to study the dynamics of biofilm growth is a finite difference scheme. We use uniform spatial and time step sizes, denoted by $\Delta y$ and $\Delta t$, respectively ~~and~~ for given solutions at time step $n-1$ and $n$ the polymer volume fraction at time step $n+1$, $\phi_n^{n+1}$ governed by the Cahn–Hilliard equation is calculated by

$$\begin{aligned} &\frac{\phi_n^{n+1} - \phi_n^n}{\Delta t} + \theta\Lambda\nabla_y^2[\Gamma_1\nabla_y^2\phi_n^{n+1} + 2\Gamma_2\chi\phi_n^{n+1}] \\ &\quad = g_n(\bar{\phi}_n^{n+\theta}, \bar{c}^{n+\theta}) - (1-\theta)\Lambda\nabla_y^2[\Gamma_1\nabla_y^2\phi_n^n + 2\Gamma_2\chi\phi_n^n] \\ &\qquad - \Lambda\nabla_y^2\Gamma_2\left(-\frac{1}{N}\ln\bar{\phi}_n^{n+\theta} + \ln(1-\bar{\phi}_n^{n+\theta})\right). \end{aligned} \tag{5.2}$$

After this, the volume fraction of the solvent at time step $n+1$ is obtained by $\phi_s^{n+1} = 1-\phi_n^{n+1}$, and the nutrient substrate concentration at time step $n+1$, $c^{n+1}$ is calculated

by

$$\begin{aligned}(5.3)\qquad &\frac{\phi_s^{n+1}c^{n+1}-\phi_s^n c^n}{\Delta t}-\theta\nabla_y\cdot(D_s\phi_s^{n+1}\nabla_y c^{n+1}-\mathbf{v}^{n+1}\phi_s^{n+1}c^{n+1})\\ &\quad=-g_c(\bar\phi_n^{n+\theta},\bar c^{n+\theta})+(1-\theta)\nabla_y\cdot(D_s\phi_s^n\nabla_y c^n-\mathbf{v}^n\phi_s^n c^n).\end{aligned}$$

The $\theta$-method is used in time discretization of both equations, where $0\le\theta\le 1$, and the spatial discretization is done using central differences to ensure the second order accuracy in space and volume preservation for $\phi_n$ when there is no polymer production. Here $\bar\phi_n^{n+\theta}=(1+\theta)\phi_n^n-\theta\phi_n^{n+1}$, $\bar c^{n+\theta}=(1+\theta)c^n-\theta c^{n+1}$ are the extrapolated values of $\phi_n$ and $c$ at time step $n+\theta$, and the nonlinear functions $g_n$, $g_c$ and the terms involving log-functions are evaluated at these extrapolated values. In our simulation throughout the paper, we use $\theta=1/2$, and thus the overall scheme is second order in time and space. The MCH equation is discretized similarly by

$$\begin{aligned}(5.4)\qquad &\frac{\phi_n^{n+1}-\phi_n^n}{\Delta t}+\theta\Lambda\nabla\cdot[\bar\phi_n^{n+\theta}\nabla_y(\Gamma_1\nabla_y^2\phi_n^{n+1}+2\Gamma_2\chi\phi_n^{n+1})]\\ &\quad=g_n(\bar\phi_n^{n+\theta},\bar c^{n+\theta})-(1-\theta)\Lambda\nabla\cdot[\phi_n^n\nabla_y(\Gamma_1\nabla_y^2\phi_n^n+2\Gamma_2\chi\phi_n^n)]\\ &\qquad-\Lambda\Gamma_2\nabla\cdot\left[\phi_n^n\nabla_y\left(-\frac{1}{N}\ln\bar\phi_n^{n+\theta}+\ln(1-\bar\phi_n^{n+\theta})\right)\right].\end{aligned}$$

Assuming that interval $I=[0,1]$ is divided into $M$ uniform subintervals of size $\Delta y=1/M$ by $M+1$ nodes $y_0,y_1,\dots,y_M$, we denote the value of the numerical solution of (5.2) and (5.3) at $(n\Delta t,j\Delta y)$ by $\phi_{n,j}^n$, $c_j^n$. Since $\mathbf{v}\cdot\mathbf{n}|_{\partial I}=\mathbf{v}_0\cdot\mathbf{n}=0$, the discrete form of the boundary conditions (5.1) is given by

$$\begin{aligned}(5.5)\qquad &\phi_{n,1}^n=\phi_{n,-1}^n,\quad \phi_{n,2}^n=\phi_{n,-2}^n,\quad \phi_{n,M+1}^n=\phi_{n,M-1}^n,\quad \phi_{n,M+2}^n=\phi_{n,M-2}^n,\\ &c_1^n=c_{-1}^n,\quad c_M^n=c^\star.\end{aligned}$$

For the purpose of completeness, we also compute the nonzero velocity components $v_x$, $v_z$ and the stress components $\tau_{xx},\tau_{xy},\dots,\tau_{zz}$, even though they are driven by $\phi_n$ and $c$. The time discretization of the equation for $v_x$ is given by

$$\begin{aligned}(5.6)\qquad &\rho^{n+1}\frac{v_x^{n+1}-v_x^n}{\Delta t}-\theta\frac{\partial}{\partial y}\left(\left(\frac{\phi_s^{n+1}}{Re_s}+\frac{\phi_n^{n+1}}{Re_p}\right)\frac{\partial v_x^{n+1}}{\partial y}\right)\\ &\quad=(1-\theta)\frac{\partial}{\partial y}\left(\left(\frac{\phi_s^n}{Re_s}+\frac{\phi_n^n}{Re_p}\right)\frac{\partial v_x^n}{\partial y}\right)+\frac{\partial(a\phi_n^n\tau_{xy}^n)}{\partial y}.\end{aligned}$$

The spatial discretization is again central difference. The discrete equation for $v_z$ is done similarly. Dirichlet boundary conditions are imposed for $v_x$ and $v_z$; i.e., $v_{x,0}^n$, $v_{xM}^n$, $v_{z,0}^n$, $v_{z,M}^n$ are given.

We note that all six components of the stress tensor satisfy a generic equation of the form

$$(5.7)\qquad \frac{\partial\tau}{\partial t}+v_y\frac{\partial\tau}{\partial y}=F(\tau,\nabla\mathbf{v}).$$

Here $F(\tau,\mathbf{v})$ has different forms for different components of the stress tensor, and it does not contain terms involving partial derivatives of $\tau$. We also note ~~here~~ that $\mathbf{v}$ can be either the polymer network velocity (JSN), the sum of the average velocity

and the excessive velocity or the average velocity (JSA), depending on the model we choose. In the following, we adopt the constitutive model using the polymer network velocity. Since $v_y = 0$ at $y = 0, 1$, there are no boundary conditions for the elastic stress tensor $\tau$; thus, $\tau$ actually satisfies an ODE: $\frac{\partial \tau}{\partial t} = F(\tau, \nabla \mathbf{v})$ at $y = 0, 1$. Then at the discrete level, we solve $\tau_0$, $\tau_M$ by the following Runge–Kutta method:

$$\tau^{n+1} = \tau^n + \frac{\Delta t}{6}(K_1 + 2K_2 + K_3 + K_4), \tag{5.8}$$

where

$$K_1 = F(\tau^n, \nabla \mathbf{v}^n), \qquad K_2 = F\left(\tau^n + \frac{\Delta t}{2}K_1, \nabla\left(\frac{\mathbf{v}^2 + \mathbf{v}^{n+1}}{2}\right)\right),$$

$$K_3 = F\left(\tau^n + \frac{\Delta t}{2}K_2, \nabla\left(\frac{\mathbf{v}^n + \mathbf{v}^{n+1}}{2}\right)\right), \quad K_4 = F(\tau^n + \Delta t K_3, \nabla \mathbf{v}^{n+1}).$$

We solve $\tau_j^n$, $1 \le j \le M - 1$, by the following upwind scheme:

$$\frac{\tau_j^{n+1} - \tau_j^n}{\Delta t} = -\frac{1}{2\Delta y}\Big\{[1 - \mathrm{sign}(v_{y,j+1/2}^n)]v_{y,j+1/2}^n(\tau_{j+1}^n - \tau_j^n) + [1 + \mathrm{sign}(v_{y,j-1/2}^2)]v_{y,j-1/2}^n(\tau_j^n - \tau_{j-1}^n)\Big\} + F(\tau_j^n, \nabla \mathbf{v}^{\mathbf{n}}). \tag{5.9}$$

**6. Numerical results and dynamics of one-dimensional biofilms.** We study the expansion and growth of one-dimensional biofilms that are homogeneous in the $(x, z)$ plane and confined to the range $0 \le y \le 1$ using the numerical scheme developed in the previous section. Table 1 lists the values of the dimensional parameters used in our simulations [7]. In the phase field model, the mobility of the polymer network is assumed a material parameter, whose value can only be calibrated through material characterization in vitro or in vivo. In this numerical study, however, we treat it as an operating parameter. Our first attempt is to characterize the effect of

TABLE 1
*Parameter values used in the simulation.*

| Symbol | Parameter | Value | Unit |
|---|---|---|---|
| $T$ | Temperature | 303 | Kelvin |
| $\gamma_1$ | Distortional energy | $1 \times 10^7$ | m kg $s^{-2}$ |
| $\gamma_2$ | Mixing free energy | $1 \times 10^{17}$ | $m^{-1}$ kg $s^{-2}$ |
| $\chi$ | Flory–Huggins parameter | 0.55 or 0.65 | dimensionless |
| $N$ | Generalized polymerization parameter | $1 \times 10^3$ | dimensionless |
| $\mu$ | Max. production rate | $1.4 \times 10^{-4}$ | $kgm^{-3}s^{-1}$ |
| $K_c$ | Half saturation constant | $5 \times 10^{-4}$ | $kgm^{-3}$ |
| $A$ | Max. consumption rate | 1 | $kgm^{-3}s^{-1}$ |
| $D_s$ | Substrate diffusion coefficient | $2.3 \times 10^{-9}$ | $m^2s^{-1}$ |
| $\eta_n$ | Viscosity due to bacteria | $4.3 \times 10^2$ | $kgm^{-1}s^{-1}$ |
| $\eta_p$ | EPS polymer network viscosity | 4.3 | $kgm^{-1}s^{-1}$ |
| $\eta_s$ | Dynamic viscosity of solvent | $1.002 \times 10^{-3}$ | $kgm^{-1}s^{-1}$ |
| $\rho_n$ | Network density | $1 \times 10^3$ | $kgm^{-3}$ |
| $\rho_s$ | Solvent density | $1 \times 10^3$ | $kgm^{-3}$ |
| $c_0$ | Characteristic substrate concentration | $1 \times 10^{-3}$ | $kgm^{-3}$ |
| $h$ | Characteristic length-scale | $1 \times 10^{-3}$ | m |
| $t_0$ | Characteristic time-scale | $1 \times 10^3$ | s |
| $a$ | Slip parameter | 0.92 | dimensionless |
| $M$ | Number of spacial subintervals | 64 | dimensionless |

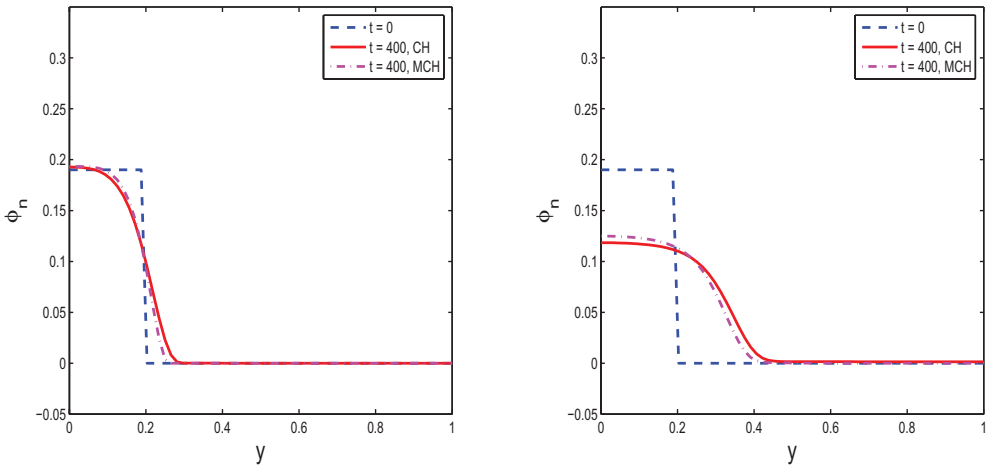


(a) $\lambda = 10^{-10}$. (b) $\lambda = 10^{-8}$.

FIG. 4. *Evolution of the polymer volume fraction in one-dimensional biofilms by the CH and MCH models without the polymer production.* $\Delta t = \Delta y$ *in* (a), $\Delta t = 0.1\Delta y$ *in* (b). *The solution is plotted at* $t = 400$. *Clearly larger mobility transports the polymer network away from the high concentration regime, reducing the volume fraction of polymers there through conservation.*

mobility on the dynamics of biofilms for both the CH and MCH models without the polymer production, i.e., $\epsilon = 0$, in which the volume fraction dynamics decouple from that of the nutrient substrate concentration. We then examine the variation of the mobility in the CH and MCH models when the polymer network production is present to select the appropriate model for our study of biofilm expansion and growth.

**6.1. Biofilm dynamics with negligible EPS production.** We begin with an initial profile of the polymer volume fraction distribution as a step function with a nonzero value at the bottom side of the domain and zero at the other side, e.g., $\phi_n(0, y) = 0.19$ for $0 \le y \le 0.2$, $\phi_n(0, y) = 0$ for $0.2 < y \le 1$. This mimics the existence of a flat layer of biofilms in a gap of thickness 1 initially. Figure 4 depicts the evolution of the polymer volume fraction in the one-dimensional biofilm according to the CH model (5.2) for different values of mobility $\lambda$. ~~T~~he horizontal axis is $y$ and the vertical axis is $\phi_n$. In each plot, the step curve is the initial profile of $\phi_n$ at $t = 0$, and the solid smooth curve is $\phi_n$ at $t = 400$. Here we choose the characteristic time-scale $t_0 = 1000$ seconds, so the dimensionless time $t = 400$ corresponds to about 4.6 days. $\lambda$ as the mobility parameter controls the magnitude of the excessive flux for the polymer network due to ~~the~~ polymer solvent mixing. We observe that when $\lambda$ is small ($\lambda = 10^{-11} \sim 10^{-10}$), the effect of the excessive flux is small and the $\phi_n$ profile is only smoothed around the initial sharp interface (discontinuity) with a slight accumulative expansion and growth, since the excessive polymer flux is not fast enough to transport the biomass out of the active mixing region. However, as $\lambda$ increases to ($10^{-9} \sim 10^{-8}$), the biomass of the polymer network is transported rapidly to the nearby polymer-scarce region leading to ~~the~~ sizable expansion of biofilms in the domain. We note that the no-flux boundary condition for $\phi_n$ at $y = 0$ and $y = 1$ leads to the total amount conservation in $\phi_n$, i.e., $\int_0^1 \phi_n(t, y)dt = \text{const}$. Accompanying the sizable expansion of the biofilm, the volume fraction of the polymer network reduces in the nonzero $\phi_n$ (or biofilm) region at larger mobility due to this conservation property.

As a comparison, Figure 4 also plots the time evolution of the polymer volume fraction in one-dimensional biofilms according to the MCH model (5.4) for a comparable set of mobility values of $\lambda$ rescaled by $\lambda \to \lambda/0.19$ to match the amount of polymeric fluxes in both models initially. The solutions of the MCH model are depicted in dot-dashed curves in the figure; they are qualitatively the same as those predicted using the CH model. However, there exists a subtle difference in the solution profile in $\phi_n$ in that the transport effect of the modified Cahn–Hilliard equation (5.4) outside the polymer-rich region is much weaker than that of the Cahn–Hilliard dynamics (5.2). This is due to the fact that the excessive polymeric flux in the MCH model is given by $-\lambda\phi_n\nabla\frac{\delta f}{\delta\phi_n}$ and vanishes when $\phi_n = 0$. On the other hand, the excessive flux in the CH model is given by $-\lambda\nabla\frac{\delta f}{\delta\phi_n}$ and may not be zero even if $\phi_n = 0$ due to the dissipative property of the CH equation and the numerical error. For example, in the case of $\lambda = 10^{-10}/0.19$, at $t = 400$, the value of $\phi_n$ at $y = 1$ is equal to 0 for the MCH model, and it is about $6 \times 10^{-5}$ for the CH model at $\lambda = 10^{-10}$. This shows that the modified Cahn–Hilliard dynamics gives a much sharper excessive flux estimation in the solvent region than the Cahn–Hilliard dynamics does, and it also maintains a sharper interface between the biofilm and the solvent. This subtlety will be amplified in the following numerical studies when the polymer network production is accounted for.

Next we study the dynamics of the biofilm expansion without polymer network production ($\epsilon = 0$) in the neighborhood of constant steady states, considering an initial polymer volume fraction profile that is the perturbation from a constant steady state, e.g., $\phi_n(0, y) = 0.19 + 0.019\cos(2\pi k y)$, where $k$ is the wave number. This transient simulation aims to investigate the nonlinear evolution of the constant steady states perturbed by either linearly stable or unstable modes. We choose two wave numbers: One falls into the linearly stable range ($k = 5$) and the other into the unstable range ($k = 3$) at $\chi = 0.65$. Our simulations demonstrate that the transient solutions corresponding to the linearly stable modes all converge to the homogenized steady state $\phi_0 = 0.19$, while the initial polymer volume fraction with the perturbation corresponding to the unstable mode evolves into a spatially inhomogeneous profile. Figure 5(a) depicts the polymer volume fraction profile corresponding to an unstable mode ($k = 3$) at $t = 400$. Since the difference in the stability between the CH and MCH models is seen only in the magnitude of the linearized growth rate, the results obtained from both models are qualitatively the same. The variation in the MCH model ~~comes slightly milder~~ than that in the CH model though. Coarsening is observed in the transient simulation.

To further illustrate the nonlinear dynamics of the biofilm in the range of unstable wave number for $\chi = 0.65$, we investigate the evolution of the biofilm with initial polymer volume fraction of a perturbation of two different wave numbers: $\phi_0(y) = 0.19 + 0.019[\cos(2\pi \cdot 3 \cdot y) + \cos(2\pi \cdot 5 \cdot y)]$, where the perturbation of the constant steady state $\phi_0 = 0.19$ contains a growth mode $k = 3$ and a decay mode $k = 5$. Figure 5(b) depicts the numerical result at $t = 400$ for both the CH and MCH models, where the shorter wave mode ($k = 5$) decays and the longer one ($k = 3$) survives and grows, confirming the linear stability analysis. The nonlinear profile calculated from the MCH model is comparable to that from model at the rescaled mobility parameter shown in Figure 5(b). Figure 5(c) portrays the evolution of the polymer volume fraction with initial condition given by a superposition of four different modes: $\phi_0(y) = 0.19 + 0.019[\xi_1\cos(2\pi 8 \cdot 2 \cdot y) + \xi_2\cos(2\pi \cdot 3 \cdot y) + \xi_3\cos(2\pi \cdot 5 \cdot y) + \xi_4\cos(2\pi \cdot 12 \cdot y)]$, where $\xi_i$, $1 \le i \le 4$, are random numbers chosen between 0 and 1. Here the perturbation contains two growth modes $k = 2, 3$ and two decay ones $k = 5, 12$. We

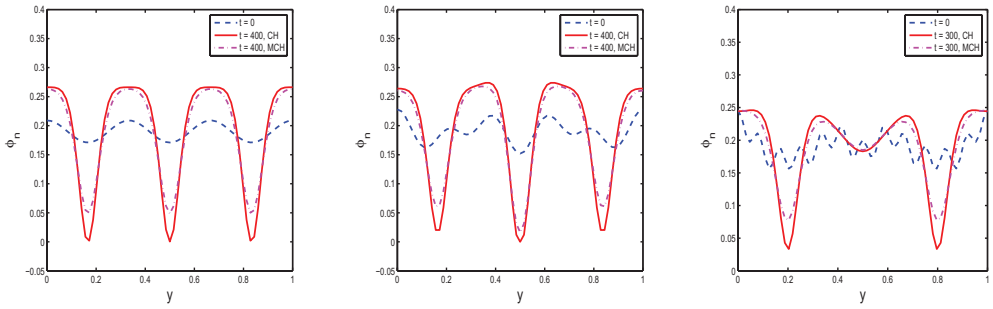


(a) one mode. (b) two modes. (c) four modes.

FIG. 5. *Evolution of the polymer volume fraction $\phi_n$ in one-dimensional biofilms by the CH and MCH models without polymer production at $\chi = 0.65$. The parameter $\lambda = 10^{-9}$. (a) The initial profile is given by $\phi_0(y) = 0.19 + 0.019\cos(2\pi k y)$, where $k = 3$. The polymer volume fraction tends to evolve (or coarsen) into islands with length-scale proportional to $1/k$. (b) The initial profile is given by $\phi_0(y) = 0.19 + 0.019[\cos(2\pi \cdot 3 \cdot y) + \cos(2\pi \cdot 5 \cdot y)]$. (c) The initial profile is given by $\phi_0(y) = 0.19 + 0.019[\xi_1 \cos(2\pi \cdot 2 \cdot y) + \xi_2 \cos(2\pi \cdot 3 \cdot y) + \xi_3 \cos(2\pi \cdot 5 \cdot y) + \xi_4 \cos(2\pi \cdot 12 \cdot y)]$, where $\xi_i$, $i = 1, \ldots, 4$, are four randomly chosen constants.*

observe that for both the CH and MCH models, the shorter waves ($k = 5, 12$) decay and the longer ones ($k = 2, 3$) grow. The profile of $\phi_n$ at $t = 300$ is a combination of the two "nonlinear modes" corresponding to $k = 2$ and $k = 3$, and the mode with $k = 3$ seems to be dominant, especially near the boundary. Note that $\beta = 2\pi k$, $k$ =2 and 3, correspond to $\beta = 12.57$ and 18.85, respectively. Figure 3(b) in section 4 indicates that the growth rate for $k = 3$ is bigger than that for $k = 2$, and thus our numerical results simply illustrate that the linear instability amplifies in the nonlinear regime.

**6.2. Biofilm dynamics with EPS production in weak shear.** Next, we turn to the growth case ($\epsilon = 1$) and study the expansion and growth of the biofilm with an initial profile of a step function in weak shear. The dimensionless shear speed at $y = 1$ is fixed at $v_x = 0.001$. The initial condition of the nutrient concentration is set at $c = c^\star = 0.03$ for $0 \le y \le 1$. Figure 6 depicts the results for the CH and MCH models. The step profile is $\phi_n$ at $t = 0$, and the smooth ones are $\phi_n$ at $t = 400$ obtained from both models. For the CH model, we observe that for small $\lambda$ ($\lambda = 10^{-11} \sim 10^{-10}$), since the excessive flux is small, the polymer network mostly grows at the position where it is initially positive, and only a very small amount is transported to the right. It is also seen that the polymer grows more rapidly around the interface between the biomass (mixture of polymer and solvent) and the pure solvent. This is because the nutrient to the left of the interface tends to all be consumed in a short period of the film growth so as to cause the polymer network growth to cease after that, but the polymer around the interface can always access the nutrient due to the nutrient diffusion at the interface. Thus, the growth near the interface can be sustained. As $\lambda$ increases (in $10^{-9} \sim 10^{-8}$), the polymer network expands into the solvent region, leading to a lower polymer volume fraction in the biofilm.

As a comparison, we repeat the same calculations using the MCH model at the same mobility parameters and the rescaled ones. Figure 6 shows the growth of the polymer volume fraction in one-dimensional biofilms according to the MCH model for the same set of values of $\lambda$ as well as the rescaled one $\lambda \to \lambda/0.19$, respectively. They are qualitatively the same as the results obtained from the CH model, but the

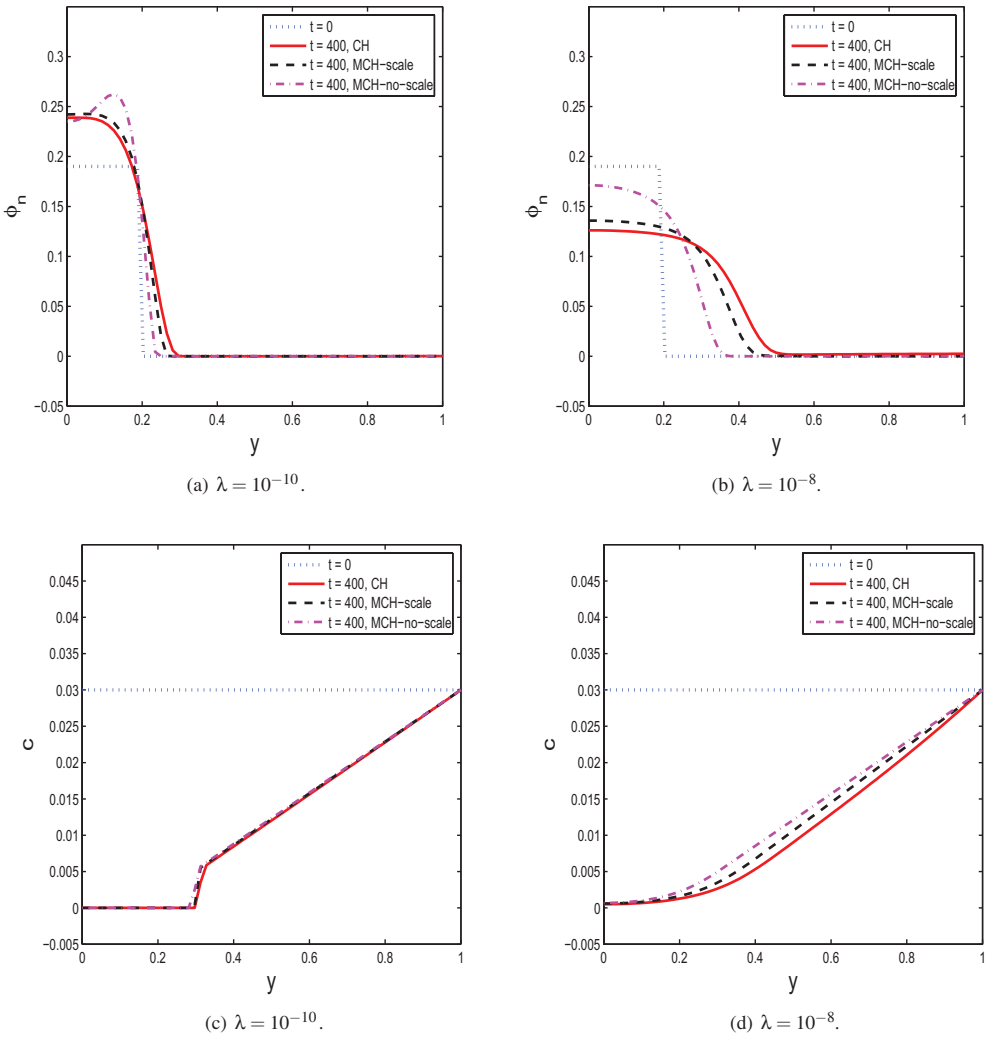


(a) $\lambda = 10^{-10}$. (b) $\lambda = 10^{-8}$.

(c) $\lambda = 10^{-10}$. (d) $\lambda = 10^{-8}$.

FIG. 6. *Growth of the polymer volume fraction in one-dimensional biofilms and the nutrient concentration profile. The parameter values are* $\epsilon = 1$, $\mu = 0.14$, $K_c = 0.5$. *The biofilm-solvent interface predicted by the MCH model always falls ~~behind~~ that ~~of~~ the CH model. In addition, the MCH model gives a more realistic estimation of the volume fraction away from the biofilm in the solvent region and allows a slightly richer supply of nutrient into the interfacial region.*

transport effect in the MCH model yields weaker polymeric fluxes. For example, the expansion of the biomass predicted by the MCH model with the rescaled mobility is slower than that ~~with~~ the CH model. In the MCH model, the one with the original (nonscaled) mobility parameter~~s~~ clearly delivers weaker polymeric flux, so that the profile of the polymer volume fraction is always higher than ~~the~~ others ~~in a majority of their nonzero region~~. Figure 6 depicts the nutrient concentration calculated from the two models with the same set of mobility parameters as well. The slightly higher nutrient concentration in the case of the MCH solution without rescaling the mobility parameter correlates well with the volume fraction profile at $t = 400$, justifying the fact that the growth is fueled by the supply of the nutrient.

In the one-dimensional situation, the average velocity, the pressure, and the elastic stress tensor components are driven dynamical variables in that their governing equations decouple from the transport equation for $\phi_n$ and $c$. We next examine the driven quantities in the one-dimensional models. First, we note that $v_y = 0$ is dictated by the continuity equation. Hence, the polymer network velocity is actually given by $(v_x, v_y^e)$. Figure 7 plots the average velocity component $v_x$ and the excessive velocity component $v_y^e$. The initial profile of $v_x$ is zero in the biofilm region and nonlinear meeting the prescribed terminal shear speed at $y = 1$. The magnitude of $v_x$ is small in the biofilm region, and all models give comparable predictions. In the solvent region, the CH model gives the largest $v_x$ while the MCH model of either rescaled or nonscaled mobility parameters is comparable at small mobility and distinct at a larger mobility value. The magnitude of $v_x$ is much smaller in the biofilm region, indicating a lack of spatial motion in the biofilm despite of the weak shear. The excessive velocity $v_y^e$ is zero in the solvent region and nonzero in biofilm at $t = 400$. The behavior of $v_y^e$ in the range of small mobility parameters is qualitatively the same. However, the velocity predicted using the MCH model differs from that of the CH model as the mobility increases. In the latter case, the velocities in $y$ predicted by the MCH are all positive, indicating a slight transient growth in the volume fraction at $t = 400$. The negative velocity in the CH model prediction indicates a transient decay of the polymer volume fraction. In all cases, the difference as well as the magnitudes are rather small (on the order of $O(10^{-4})$).

Figure 7 also depicts the normal stress component $\phi_n \tau_{yy}$, where the JSN model with $a = 0.92$ is used. The normal stress components predicted by the three models are similar qualitatively at small mobility parameter $\lambda = 10^{-10}$, where the stress component exhibits a peak in the middle of the biofilm region and a negative value at the biofilm-solvent interface. The same qualitative behavior can be described for the pressure. At higher mobility values, the stress component and the pressure calculated from the CH model yields the largest stress fluctuation in a neighborhood of the interface. The stress obtained from the MCH model with rescaled and nonscaled mobility parameters shows larger numerical value in the biofilm region and smaller fluctuation across the interface. The CH model predicts a stress and pressure undershoot followed by an overshoot in the biofilm region near the interface. Since the transport equation for the polymer volume fraction impacts the polymer network velocity, which in turn drives the polymer elastic stress as well as the pressure, the drasticly different behavior is another manifestation of the velocity difference in $v_y^e$ near the interface.

We have contrasted the prediction of the CH model with that of the MCH model. One question remains: Which one is better suited for modeling biofilms numerically? In the CH model, the polymeric flux is completely controlled by the variation of the free energy density, while it depends on both the polymer volume fraction and the free energy density variation in the MCH model. Figure 8 depicts the computed profile of the polymer volume fraction in one-dimensional biofilms with a higher nutrient concentration $c^\star = 0.2$ at $y = 1$ and two different mobility parameters. The higher concentration tends to speed up the polymer network expansion and growth across the entire domain. For the CH model, when $t$ is small, we observe that the polymer network grows due to the production term and expands to the solvent region due to the excessive polymeric flux. As $t$ increases, $\phi_n$ becomes nonzero at $y = 1$ due to the numerical dissipation and the truncation errors. When $\phi_n$ becomes nonzero at $y = 1$, an exponential growth ensues due to growth rate $g_n$ in the governing equation for $\phi_n$ and soon reaches 1, causing our computations to break down. The value of $\phi_n$ at $y = 1$ reaches 1 faster for $\lambda = 10^{-9}$ (shortly after $t = 260$) than for $\lambda = 10^{-10}$

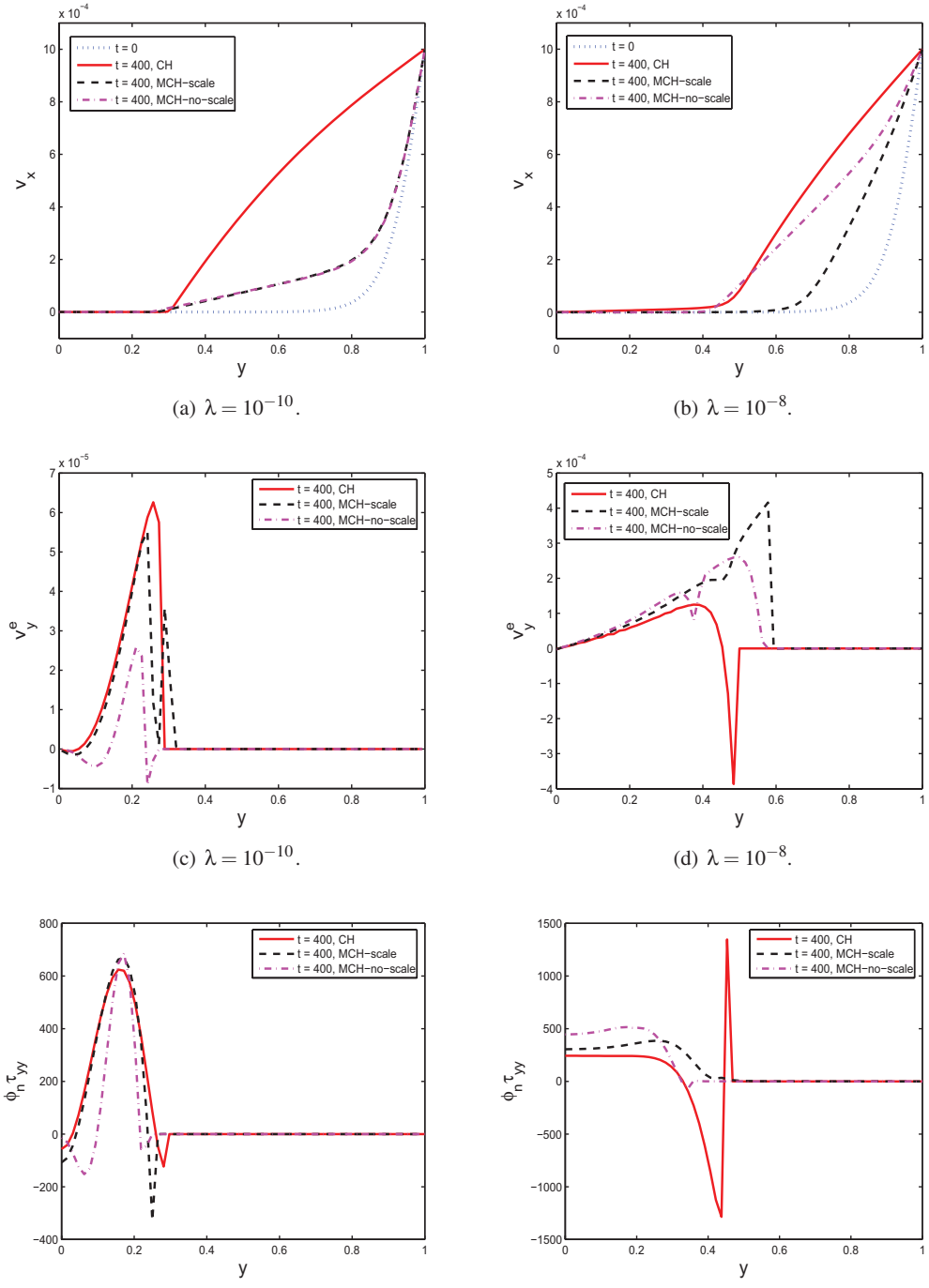


(a) $\lambda = 10^{-10}$. (b) $\lambda = 10^{-8}$.

(c) $\lambda = 10^{-10}$. (d) $\lambda = 10^{-8}$.

(e) $\lambda = 10^{-10}$. (f) $\lambda = 10^{-8}$.

FIG. 7. *The profile of the average velocity* $\mathbf{v}_x$, $v_y^e$ *and the elastic stress component* $\phi_n \tau_{yy}$ *in the one-dimensional biofilm and solvent mixture.*

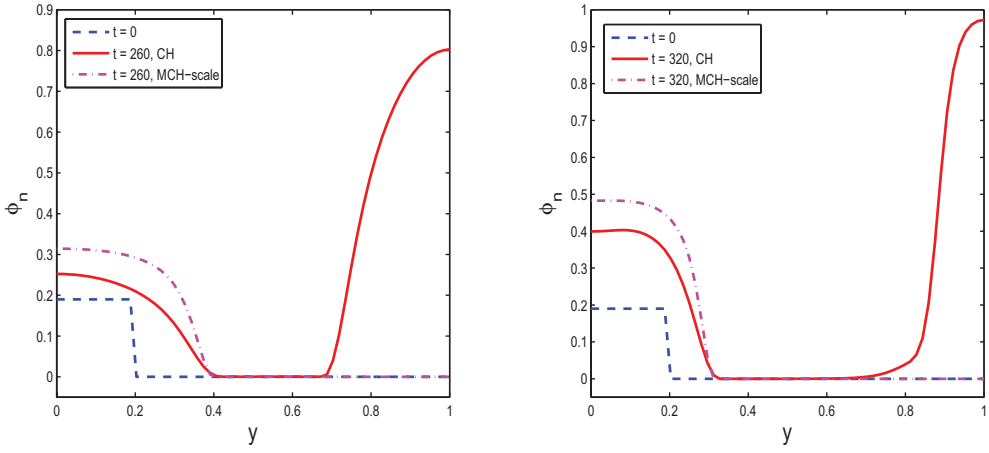


(a) $\lambda = 10^{-9}$. (b) $\lambda = 10^{-10}$.

FIG. 8. *Growth of the polymer volume fraction in one-dimensional biofilms with a higher nutrient concentration $c^\star = 0.2$. For CH model, the numerically generated artificial growth at the top boundary disqualifies the model when polymer production is present. The MCH model renders physically correct prediction in the nutrient-rich solvent, making it our choice of models for studying fluid mixtures.*

(shortly after $t = 320$). This numerical evidence demonstrates the limitation of the CH model in modeling the polymer production numerically. The MCH model, on the other hand, does not suffer the unphysically numerical growth of $\phi_n$ at $y = 1$, since the polymeric flux near $y = 1$ vanishes due to $\phi_n = 0$ in the pure solvent region. Numerically, the zero polymeric flux condition in the solvent region is much easier to maintain in the MCH model before the growth reaches the boundary than in the CH model. We also notice that $\phi_n$ grows faster near the original interface in the MCH model than in the CH model. This is because once $\phi_n$ starts to grow at $y = 1$ in the CH model, the nutrient is consumed there quickly, which in turn reduces the amount of the nutrient being diffused to the original interface and thus reduces the polymer production rate. Physically, the MCH model is based on a better assumption on the polymeric flux. The above numerical result hence supports that the MCH model is more appropriate for modeling the transport of the polymer network for its accurate modeling of the transport of the polymeric flux than the CH model.

Finally, we investigate the expansion and growth of an inhomogeneous biofilm initially located at one side of the domain, shown in Figure 9, using the MCH model. When the initial profile contains unstable long wave modes, the dominating growth occurs in the biofilm region with significant coarsening and little expansion into the solvent region initially. In this calculation, we solve the governing system of equations at $\chi = 0.65$ using the MCH model for an extended period of time. Figure 9 depicts the expansion and growth of biofilms from perturbed initial data calculated by the MCH (with the rescaled mobility) model at two different values of nutrient-supply boundary value $c^\star$ and for sufficiently long time. Figure 9(a) and (b) show the $\phi_n$ and $c$ ~~profile~~ for $c^\star = 0.03$ at five different times. Since $\chi = 0.65$, we know that there are some long wave unstable modes from the linear stability analysis to fuel the expansion and growth of the biofilm. For relatively short time ($t \leq 400$), we observe that the long wave to the left of the interface grows, and the polymer volume fraction profile undergoes a sharp transition near the interface, pulling the polymer network to the

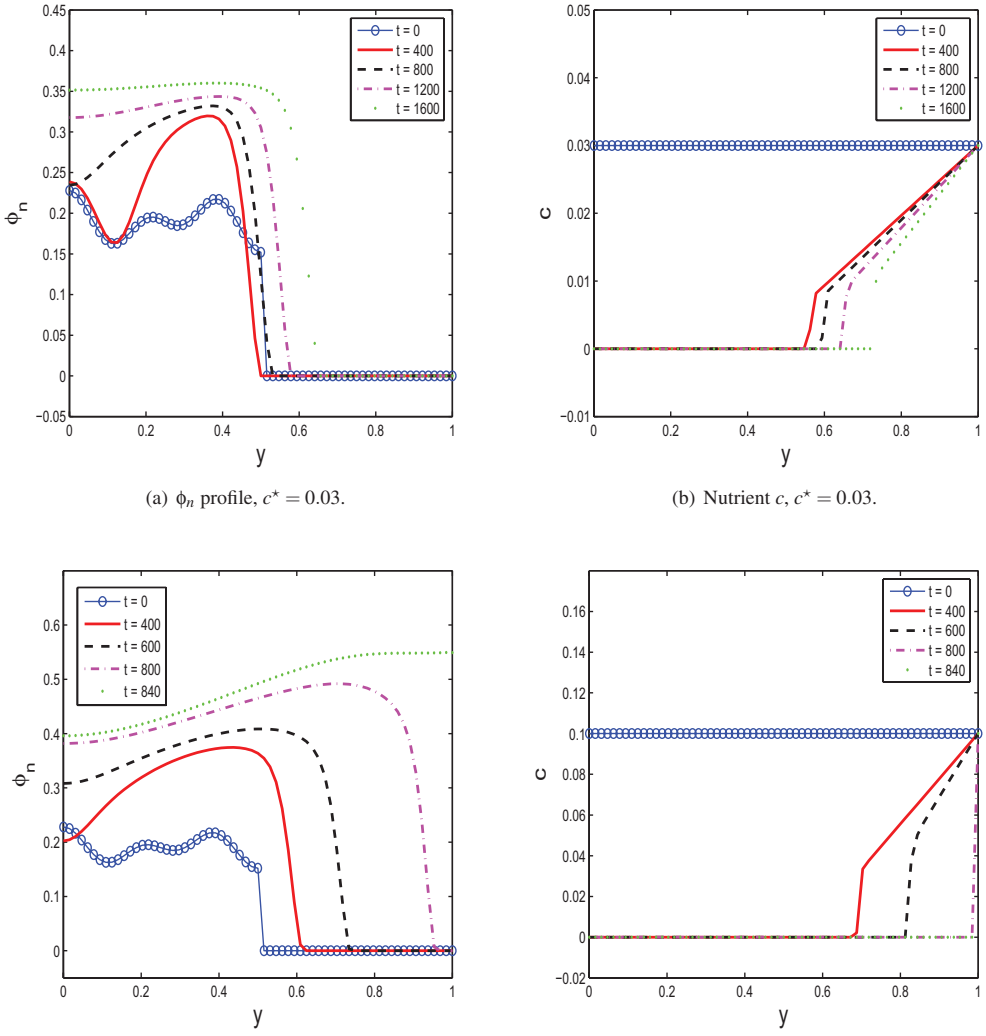


(a) $\phi_n$ profile, $c^\star = 0.03$.

(b) Nutrient $c$, $c^\star = 0.03$.

(c) $\phi_n$ profile, $c^\star = 0.1$.

(d) Nutrient $c$, $c^\star = 0.1$.

FIG. 9. *The polymer volume fraction $\phi_n$ and nutrient concentration $c$ computed by the MCH model with a perturbed initial data with growth for two different $c^\star$, simulated for a sufficiently long time. The parameter values are $\chi = 0.65$, $c^\star = 0.03, 0.1$, $\lambda = 10^{-9}$, $\phi_0(y) = 0.19 + 0.019[\cos(2\pi \cdot 3 \cdot y) + \cos(2\pi \cdot 5 \cdot y)]$ for $y \le 0.5$, $\phi_0(y) = 0$ for $y > 0.5$. After an initial pulling back, the biofilm expands into the solvent region as long as there is a continuous supply of nutrient.*

biofilm-rich region relative to the initial profile. An intuitive explanation for this is that due to the weaker dissipation in the model, the rapid growth of the polymer network and coarsening in the biofilm draw the polymers near the interface into the polymer-rich region, a consequence of the long wave instability. The pulling back phenomenon is clearly tied to the coarsening, because the nutrient concentration at $t = 400$ is nearly zero in the biofilm region shown in the figure. As time ~~increases~~, we observe that the profile of the polymer volume fraction in the biofilm tends to level off, or coarsening ceases, so that the growth of the polymer network becomes more uniform away from the biofilm-solvent interface and the interface starts to expand into the solvent. From the bulk free energy density $\hat{f}(\phi_n)$, we can see that the bulk contribution

to the polymer network flux decreases as the volume fraction $\phi_n$ continuously grows. At a lower polymer volume fraction, the expansion of the biofilm is facilitated by the bulk free energy along with the conformational free energy tied to the curvature of the interface profile of $\phi_n$. As the polymer volume fraction exceeds a critical value though (zero of $\frac{\partial^2 \hat{f}}{\partial \phi_n^2} = 0$), the driving force behind the expansion is due purely to the curvature effect.

We also examine the nutrient distribution during the above-mentioned process. We notice that the nutrient tends to be depleted within the biofilm as the polymer network tends to reach a uniform distribution; however, the nutrient supply is sufficient at the biofilm-solvent interface fueling the expansion and growth of the polymer network continuously outwards. This explains the dynamics of the polymer network expansion in biofilms for long times. Figure 9(c) and (d) depict the results for a higher nutrient concentration at $c^\star = 0.1$. They are qualitatively the same as the case of $c^\star = 0.03$, except that the dynamics take place at a much faster pace here.

**7. Conclusions.** In this paper, we present a phase field theory modeling biofilm and solvent mixtures as incompressible complex fluids. In this one-fluid two-component theory, the extracellular polymeric substance (EPS) along with the bacteria is treated as one effective viscous or viscoelastic component, and the nutrient and the solvent are treated as the other effective viscous component. The growth of the effective polymer network component is modeled by a saturated growth, while the nutrient consumption is approximated by a linear decay. Three constitutive models for the mixture are proposed: Extended Newtonian, rubber elastic gel, and viscoelastic model. That the mixture in the bulk is incompressible leads to a divergence-free averaged velocity field. The interpenetrating between the two effective components is measured by the excessive velocities accounted for by the Flory–Huggins polymer mixing dynamics. Surface tension between the pure solvent section of the solvent fluid and the biofilm is naturally built in through a nonlocal entropic mixing free energy density. The Cahn–Hilliard dynamics coupled with the Flory–Huggins mixing is investigated with respect to various mobility parameters. Modified Cahn–Hilliard dynamical transport is shown to be more appropriate for the biofilm expansion and growth, which can effectively eliminate the unwanted and unphysical growth in the solvent region due to the numerical error and dissipation.

There are a limited number of results that can be used to validate the model presently. One of the results used in a few reports [8, 13, 27] is that the flat biofilm-fluid interfaces are unstable for a finite interval of perturbation modes, with a single maximally unstable mode. Both the linear analysis and the nonlinear simulations of the present model confirm these predictions.

The advantage of modeling biofilms using a multicomponent material includes robust treatment of the physics and interacting dynamics among the components. Meanwhile, deriving a model consisting of a single fluid eliminates several difficulties associated with the coupled biofilm-bulk fluid flow like velocity, boundary conditions, etc. In particular, the interface conditions are dramatically simplified, since the interface is not separated from the rest of the system. In addition, influent and effluent boundary conditions are natural in the single fluid case. The present treatment also provides a framework in which various constitutive relations for each constituent can be investigated in conjunction with the motion of the bulk fluid. Both of these are important in order to address dispersal, detachment, and sloughing events which have substantial impact in industrial and medical settings of the biofilm.

## REFERENCES


[1] E. Alpkvist and I. Klapper, *A Multidimensional Multispecies Continuum Model for Heterogeneous Biofilm Development*, preprint, 2005.

[2] A. N. Beris and B. Edwards, *Thermodynamics of Flowing Systems*, Oxford Science Publications, New York, 1994.

[3] R. B. Bird, R. C. Armstrong, and O. Hassager, *Dynamics of Polymeric Liquids*, Vol. 1 & 2, John Wiley and Sons, New York, 1987.

[4] J. W. Cahn and J. E. Hilliard, *Free energy of a nonuniform system.* I: *Interfacial free energy*, J. Chem. Phys., 28 (1958), pp. 258–267.

[5] J. W. Cahn and J. E. Hilliard, *Free energy of a nonuniform system—*III: *Nucleation in a* 2*-component incompressible fluid*, J. Chem. Phys., 31, (1959), pp. 688–699.

[6] P. M. Chaikin and T. C. Lubensky, *Principles of Condensed Matter Physics*, Cambridge University Press, Cambridge, UK, 1995.

[7] N. G. Cogan and J. P. Keener, *Channel formation in gels*, SIAM J. Appl. Math., 65 (2005), pp. 1839–1854.

[8] N. Cogan and J. Keener, *The role of biofilm matrix in structural sevelopment*, Math. Med. Biol., 21 (2004), pp. 147–166.

[9] J. W. Costerton, Z. Lewandowski, D. E. Caldwell, D. R. Korber, and H. M. Lappin-Scott, *Microbial biofilms*, Annu. Rev. Microbiol., 49 (1995), 711745.

[10] B. Costerton, *Medical Biofilm Microbiology: The Role of Microbial Biofilms in Disease, Chronic Infections, and Medical Device Failure*, CD-ROM, Montana State University, Bozeman, MT, 2003.

[11] M. E. Davey and G. A. O'Toole, *Microbial biofilms: From ecology to molecular genetics*, Microbiol. Molec. Biol. Rev., 64 (2000), pp. 847–867.

[12] E. De Lancey Pulcini, *Bacterial biofilms: A review of current research*, Nephrologie, 22 (2001), pp. 439–441.

[13] J. Dockery and I. Klapper, *Finger formation in biofilm layers*, SIAM J. Appl. Math., 62 (2001), pp. 853–869.

[14] M. Doi and S. F. Edwards, *The Theory of Polymer Dynamics*, Oxford Science Publications, Oxford, UK, 1986.

[15] M. Doi, *Introduction to Polymer Physics*, Oxford Science Publications, Oxford, UK, 1995.

[16] P. J. Flory, *Principles of Polymer Chemistry*, Cornell University Press, Ithaca, NY, 1953.

[17] D. J. Hassett, P. A. Limbach, R. F. Hennigan, K. E. Klose, R. E. Hancock, M. D. Platt, and D. F. Hunt, *Bacterial biofilms of importance to medicine and bioterrorism: Proteomic techniques to identify novel vaccine components and drug targets*, Expert Opin. Biol. Ther., 3 (2003), pp. 1201–1207.

[18] R. G. Larson, *The Rheology of Complex Fluids*, Oxford University Press, New York, 1998.

[19] C. A. A. Lima, R. Ribeiro, E. Foresti, and M. Zaiat, *Morphological Study of Biomass During the Start-Up Period of a Fixed-Bed Anaerobic Reactor Treating Domestic Sewage*, Brazilian Archives of Biology and Technology

[20] I. Klapper, *Effect of heterogeneous structure in mechanically unstressed biofilms on overall growth*, Bull. Math. Biol., 66 (2004), pp. 809–824.

[21] I Klapper, C. J. Rupp, R. Cargo, B. Purvedorj, and P. Stoodley, *Viscoelastic fluid description of bacterial biofilm material properties*, Biotech. Bioeng., 80 (2002), pp. 289–296.

[22] I. Klapper and J. Dockery, *Role of cohesion in the material description of biofilms*, Phys. Rev. E, 74 (2006), paper 031902.

[23] C. S. Laspidou and B. E. Rittmann, *Modeling biofilm complexity by including active and inert biomass and extracelluar polymeric substances*, Biofilm, 1 (2004), pp. 285–291.

[24] J. Lowengrub and L. Truskinovsky, *Quasi-incompressible Cahn–Hilliard fluids and topological transitions*, R. Soc. Lond. Proc. Ser. A Math. Phys. Eng. Sci., 454 (1998), pp. 2617–2654.

[25] S. T. Milner, *Dynamical theory of concentration fluctuations in polymer solutions under shear*, Phys. Rev. E, 48 (1993), pp. 3674–3691.

[26] G. O'Toole, H. B. Kaplan, and R. Kolter, *Biofilm formation as microbial development*, Ann. Rev. Microbiol., 54 (2000), pp. 49–79.

[27] C. Picioreanu, M. van Loosdrecht, and J. Heijnen, *Mathematical modeling of biofilm structure with a hybrid differential-discrete cellular automaton approach*, Biotech. Bioeng., 58 (1998), 101116.

[28] C. Picioreanu, M. van Loosdrecht, and J. Heijnen, *Multidimensional modelling of biofilm structure*, Biotech. Microbial Biosystems: New Frontiers, Proceedings of the 8th Interna-

tional Symposium on Microbial Ecology, C. R. Bell, M. Brylinsky, and P. Johnson-Green, eds., Atlantic Canada Society for Microbial Ecology, Halifax, NS, Canada, 1999.

[29] C. Picioreanu, M. J-U Kreft, and M. van Loosdrecht, *Particle-based multidimensional multispecies biofilm models*, Appl. Environ. Microbiol., May (2004), pp. 3024–3040.

[30] C. Picioreanu, J. B. Xavier, and M. van Loosdrecht, *Advances in mathematical modeling of biofilm structure*, Biofilm, 1 (2004), pp. 337–349.

[31] H. Tanaka, *Viscoelastic model of phase separation*, Phys. Rev. E, 56 (1997), pp. 4451–4462.

[32] O. Wanner and W. Gujer, *A multispecies biofilm model*, Biotech. Bioeng., 28 (1986), pp. 314–328.

[33] C. Wolgemuth, E. Hoiczyk, D. Kaiser, and G. Oster, *How Myxobacteria glide*, Current Biol., 12 (2002), pp. 369–377.